University of Basel
Faculty of Science
Departement of Physics

Optical Coherence of Colour-Defects in Diamond

Master's Thesis by

Josh A. Zuber

Supervised by:

Prof. Dr. Patrick Maletinsky

Dr. Marcel·lí Grimau Puigibert

Dr. Mark Kasperczyk

Basel, January 31, 2020

Abstract

In this thesis the optical coherence of two prominent colour defects in diamond, the nitrogen-vacancy (NV) centre and the silicon-vacancy (SiV) centre, are investigated with distinct methodologies. For the NV centre, we probe a sample at low temperature that has been implanted with ^{15}N ions after nano-structuring, permitting isotopic labelling of the optical coherence properties of the centres by pulsed optically detected magnetic resonance and statistical analysis of the dataset. We find that for a sample size of 51 NV centres, no defect formed from implanted nitrogen exhibits coherent emission with linewidths below 1 GHz, whereas centres formed from naturally abundant ^{14}N consistently show narrow, and thus coherent, emission.

For the SiV centre, we investigate the optical properties at both ambient conditions and 4 K for shallow (∼50 nm from the surface) defects in diamond nano-pillars, establishing that the SiV can show consistent coherent emission with linewidths below 1 GHz even in nano-structures. Our study also briefly evaluates the fabrication parameters that will result in optically coherent single SiV centres in nano-pillars. Additionally, we analyse the physics of the defect and evaluate its potential as a magnetometer for applications at ultra-low temperature and high magnetic field conditions by estimating sensitivities to dc-magnetic fields for two distinct sensing protocols.

Acknowledgements

First of all, I would like to thank Patrick Maletinsky for the opportunity to be a member of the Quantum Sensing lab in Basel, for his guidance throughout my project and his contagious enthusiasm for physics, always sparking new ideas and motivation. I am deeply indebted and grateful to both Marcel·lí Grimau and Mark Kasperczyk, who never grew tired of explaining our experiments to me, helping me align setups and answering all possible and impossible questions a Master's student could or could not have. Working in the dark lab was a lot brighter with your guidance and I am looking forward to the future!
A big thank you also to Jodok Happacher who always had a helping hand and valuable, pedagogical advice or tasks for me and who introduced me to coding (passable) GUIs in Matlab. Furthermore, I am thankful to all members of the Quantum Sensing group for welcoming me in their ranks and the invaluable advice and help each one of them provided.

Last but not at all least, I would like to thank my friends and my family for always having my back, believing in me and helping me believe in myself. I could not have become a physicist (or be on the way to becoming one) without André and Luzia, my parents, my siblings Grace, Amy, Luna and Mike (who, as always, read my manuscript and provided desperately needed linguistic advice), and I surely would not have made it without Saphira, who was always with me, every step of the way. Thank you!

Contents

Introduction

In recent years, colour centres in diamond, which are point defects within the crystal lattice that absorb and emit certain wavelengths of light, have received considerable attention in the context of both the emerging field of quantum sensing and the field of quantum information.[1,2] Although there are various different colour centres in diamond, the most prominent and thoroughly investigated example is the negatively charged nitrogen-vacancy (NV) centre, which exhibits a highly coherent and optically addressable spin, making it a prominent candidate for quantum information and quantum sensing protocols.[3] Indeed, entanglement and subsequently quantum teleportation and Bell inequality violations,[4,5,6] as well as quantitative nano-magnetometry of 2D materials and all optical nano-thermometry have been demonstrated with NV centre spins.[7,8,9]
However, while its spin properties are outstanding, the NV centre exhibits several shortcomings in its optical emission, such as long radiative lifetimes of ∼12 ns or a Debye-Waller factor (the ratio between the intensity of zero-phonon line (ZPL) emission and the overall intensity of the emitter emission) of around 3-4%, among others. These shortcomings prevent high fidelity quantum information protocols and up-scaling to extended quantum networks. In principle, these issues can be addressed by incorporating the NV centre in an optical cavity; however, the diamond nano-structuring necessary to do so introduces large homogeneous broadening of the NV's ZPL, inhibiting the NV's use as a source of single, indistinguishable photons.[10]
The broadening of the line after fabrication is attributed to the damage induced to the lattice by ion-implantation, which is, in combination with high-temperature annealing, a widely used method to create NV centres.[11] Indeed, all experiments using coherent photons from NV centres have employed NV centres formed during diamond growth. It is furthermore suggested that NV centres created from implanted nitrogen ions lack the optical coherence of their intrinsic counterparts altogether.[12]

Conversely, another colour centre in diamond exhibits advantageous optical properties without the need for an optical cavity: the negatively charged silicon-vacancy (SiV) centre. The SiV exhibits a Debye-Waller factor of above 75%,[13] a short optical lifetime of around 1 ns,[14] and low spectral diffusion because of its inversion symmetry.[15] It generally seems that for solid-state spin systems, good optical properties go hand in hand with poor spin-coherence and vice-versa, and the SiV is no exception to this rule with a spin coherence time of only ∼100 ns at 4 K, limited by a single-phonon orbital relaxation process.[16] However, the SiV could prove to be a promising building block for spin-photon interfaces at ultra-low temperatures, combining both desirable optical and spin behaviour in this regime, with spin coherence times of 13 ms at 100 mK.[17,18] The SiV centre, then, is an interesting alternative to the NV centre in the realm of ultra-low temperature magnetometry, especially since all-optical control of the spin is not limited to specific bias-field values or other restricting and complicating requirements as it is the case for the NV centre.[19,20] Indeed, all-optical control of the SiV centre's spin states

at temperatures as low as 40 mK has recently been demonstrated,[21] paving the way for high-field single-spin magnetometry at ultra-low temperatures.

In this thesis, we conduct two experiments: In the first, we further explore the effect of ion-implantation on optical coherence of NV centre photons by reversing the usually employed order in sample fabrication. We fabricate nano-structures (membranes and cantilevers) before implantation of nitrogen ions. Additionally, instead of the naturally abundant ^{14}N isotope, we implant ^{15}N, permitting isotopic labelling of the NVs to distinguish defects formed from naturally occurring ^{14}N from defects formed from implanted ^{15}N.
In the second experiment, we investigate the optical properties of SiV centres in diamond-nanopillars at both room-temperature and 4 K to lay the foundations for scanning-probe magnetometry at ultra-low temperatures. Additionally, we perform numerical calculations to gain a better understanding of the photophysics of the SiV centre. We also evaluate the use of the SiV as a sensor by proposing two distinct magnetic field sensing protocols and estimating their sensitivity to dc-magnetic fields.

The thesis is structured as follows: In the first chapter, we introduce the photophysics of both the NV and the SiV centre to set the stage for the experiments, described in the third chapter. The second chapter concerns the low-temperature setup and the samples that we examined. Finally, in the fourth chapter, we summarise our results and provide an outlook for future investigations.

This project was carried out in Prof. Dr. Patrick Maletinsky's Quantum Sensing lab at the University of Basel. During the course of this thesis, I will also be presenting data collected by other members of the Quantum Sensing lab, or in collaboration with them. The design and statistical analysis of the NV experiment are due to Dr. Mark Kasperczyk; data were collected in collaboration. Dr. Brendan Shields and Dr. Marcel·lí Grimau provided the SiV sample. Room-temperature and low-temperature measurements with SiVs were conducted in collaboration with Dr. Marcel·lí Grimau.

Chapter 1

Colour Centres in Diamond

The following chapter introduces both the NV centre and the SiV centre, comparing their respective physical properties and setting the stage for the experiments to be discussed in Chap. 3. Sect. 1.1 presents the structure and photophysics of the NV centre and Sect. 1.2.1 does the same for the SiV centre. Finally, in Sect. 1.2.2, a model is introduced that reproduces the essential physics of the SiV centre.

1.1 The Nitrogen-Vacancy Centre

1.1.1 Structure and Photophysics

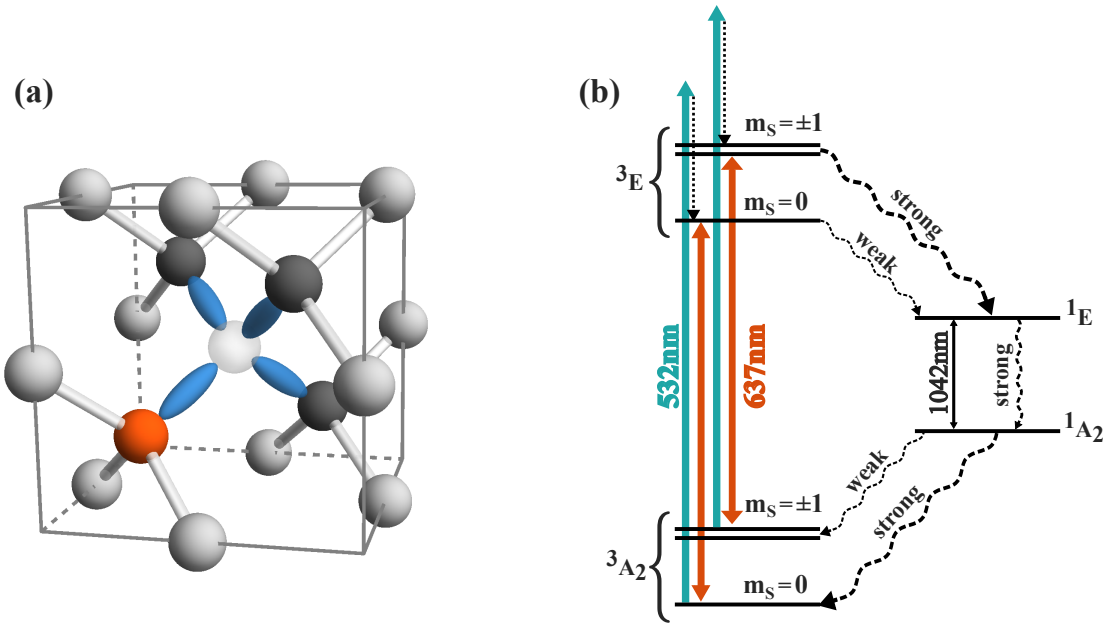

Fig. 1: **(a)** Diagram of the diamond lattice with a NV centre defect. Nearest-neighbour carbon atoms are depicted in dark grey, the substitutional nitrogen atom in red, and the vacancy transparently. Blue is used to represent the dangling bonds of the nearest-neighbour atoms of the vacancy. **(b)** Energy-level diagram of NV^-, including the room-temperature fine structure of the electronic ground and excited triplet state (magnetic quantum number $m_S \in \{0, \pm 1\}$), denoted with $^3A_2$ and ^3E. In addition, there are transitions involving the singlet states ^1E and $^1A_2$. The green and red solid arrows represent the off-resonant or resonant excitation wavelengths between the triplet states (dotted straight arrows denote non-radiative decays from vibrational states into ^3E), while the black solid arrow shows the infra-red transition between the singlet states. Dotted, wavy arrows represent non-radiative decay channels, constituting the intersystem crossing (ISC) in the NV centre.

The NV centre is an atom-like point defect with C_{3v} symmetry in diamond, consisting of a lattice vacancy and a substitutional nitrogen atom paired together as nearest neighbours. Its structure within the diamond lattice is depicted in Fig. 1(a). There are three known charge states of the NV, the negatively charged NV^-, the neutral NV^0, and the positively charged NV^+. The neutral and negative charge states can be identified by their optical zero-phonon lines (ZPLs) at 637 nm (see Fig. 2(b) for a room-temperature optical spectrum) and 575 nm respectively; NV^+ currently lacks comparable magnetic or optical signatures, and its features remain elusive.[22] Although the NV charge states fluctuates between NV^- and NV^0 even during a single measurement, little is known about the neutral state, and its fine structure has only recently been observed.[23] Thus, if not specified otherwise, we refer to NV^- simply as NV, since our investigation is focused on this charge state.

The NV centre orbital states are occupied by six electrons, two originating from the substitutional nitrogen atom, one each from the dangling bonds of the three neighbouring carbon atoms and one additional electron, typically donated by nearby lattice-impurities or other dopants.[3]
The main features of the optical properties of the NV are captured by a relatively simple model, consisting of eight electronic states as depicted in Fig. 1(b). The ^3E and $^3A_2$ levels, linked by the resonant transitional wavelength of 637 nm, are spin-triplet states, with three possible spin projections $m_S \in \{0, \pm 1\}$ along the NV spin quantisation axis, set by the symmetry axis of the defect. The ^1E and $^1A_2$ levels, linked by an infra-red transition corresponding to 1042 nm, are spin singlets. A zero-field splitting originating from spin-spin interactions[3] splits the $|m_S = 0\rangle$ state from the $|m_S = \pm 1\rangle$ by $D_g = 2.88$ GHz in the ground state. The corresponding splitting in the excited state accounts to $D_e = 1.42$ GHz.[24]

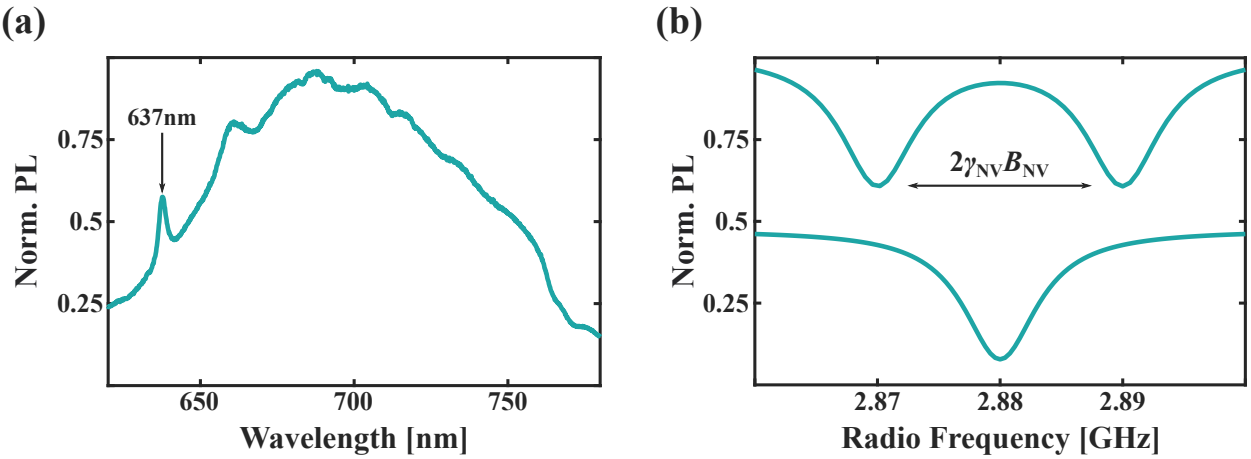

Fig. 2: **(a)** An optical spectrum of the NV centre excited with a 532 nm laser at room temperature, showing the characteristic ZPL at 637 nm and the strong phonon sideband (PSB) ranging from 640 nm to 780 nm. **(b)** Calculated ODMR spectra of the ground-state of a single NV centre showing a single resonance in zero-field conditions and two resonant lines due to the Zeeman effect when an external static magnetic field is applied (the two spectra are shifted vertically for clarity). The distance between the two resonance lines depends linearly on the projection to the NV-axis of the field applied to the defect and is given by $2\gamma_{NV} B_{NV}$, where $\gamma_{NV} = g\mu_B$ is the gyromagnetic ratio, μ_B is the Bohr magneton, g the electron g-factor, and B_{NV} is the projection of the applied magnetic field to the NV-axis.[25]

As indicated in Fig. 1(a), the NV can be off-resonantly excited by a 532 nm laser, populating vibrational states slightly higher in energy than the ^3E state. The population then decays non-radiatively into the excited-state manifold. Once ^3E is populated, there are two relaxation pathways, one of which is an optical transition

producing red photoluminescence (PL) and the other a non-radiative intersystem crossing (ISC) to the defect's singlet states.[26] The ISC pathway plays an essential role in the spin-photo dynamics of the NV centre: Optical transitions are primarily spin-conserving (i.e. they obey the selection rule $\Delta m_S = 0$); however, this is not the case for the non-radiative ISC. Indeed, this decay-path is highly spin-selective and mainly allowed from the $|m_S = \pm 1\rangle$ sublevel of the excited state as indicated by Fig. 1(b). On the contrary, the non-radiative decay from the $^1A_2$ singlet state favours the $|m_S = 0\rangle$ sublevel of the ground state, providing optical pumping of the electron spin into $|m_S = 0\rangle$. Additionally, the non-radiative nature of the ISC results in a spin-dependent PL intensity, which is significantly higher when the $|m_S = 0\rangle$ state is populated. This effect originates from much higher shelving rates of the $|m_S = \pm 1\rangle$ sublevels than of the $|m_S = 0\rangle$ sublevel.[26] This permits optically detected magnetic resonance (ODMR) of a single NV spin, to be performed as follows:
A single NV centre is prepared in the $m_S = 0$ ground state by optical pumping. Applying a resonant microwave (MW) field to the defect drives the $|0\rangle_g \longleftrightarrow |\pm 1\rangle_g$ (the subscript denoting the ground state) transition and the spin-conserving optical transition excites the NV into the excited state. Since now a significant percentage of the spin-population is pumped into the $|\pm 1\rangle_e$ state with its high shelving rate, a drop in PL can be observed (as shown in calculated ODMR spectra depicted in Fig. 2(b)).[26]

The method of performing ODMR is extensively used in both quantum information processing[27] and in single-spin magnetometry.[26] Indeed, the Zeeman effect lifts the degeneracy of the $|\pm 1\rangle$ states in the presence of an applied magnetic field, leading to two resonant dips in the ODMR spectrum, whose frequency spacing is directly proportional to the magnetic field applied to the NV centre (cf. Fig. 2(b)).[26]

Continuous wave (cw) ODMR experiments are useful to determine the energy of the $|0\rangle \longleftrightarrow |\pm 1\rangle$ transitions. In general, pulsed spin-manipulation protocols can be used to probe the hyperfine structure of the NV centre, revealing the interaction between its electronic and nuclear spin as well as interactions with carbon atoms of the diamond lattice. It is not possible to resolve these interactions by cw spin-manipulation experiments due to their limited spectral resolving power, but reducing the duty-cycle by pulsing remedies this issue. Indeed, such protocols can be used to investigate the properties of the NV centre (for example, the nuclear spin of the nitrogen atom the NV is formed from) and of its environment.[28] We will perform pulsed ODMR (pODMR) measurements to determine the nitrogen isotope of NV centres to distinguish intrinsic NV centres (formed from naturally abundant ^{14}N) from NV centres created from implanted ^{15}N (cf. Sect. 3.1).

1.2 The Silicon-Vacancy Centre

1.2.1 Structure and Photophysics

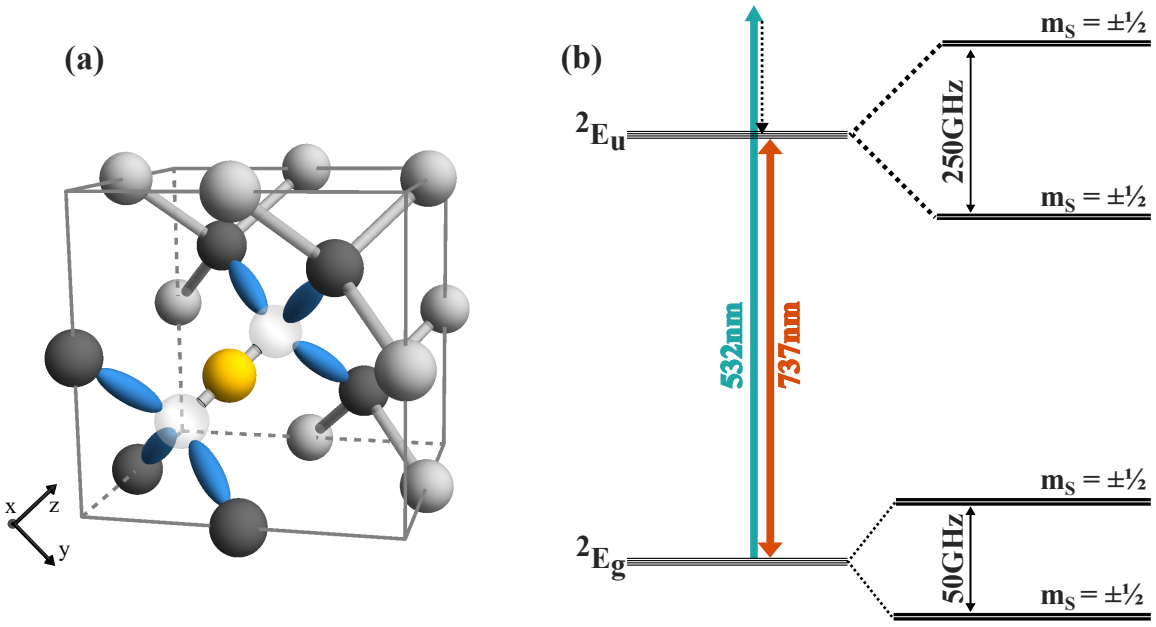

Fig. 3: **(a)** Diagram of the diamond lattice with a SiV centre defect. Nearest-neighbour carbon atoms are depicted in dark grey, the substitutional silicon atom in yellow, and the vacancy transparently. Blue is used to represent the dangling bonds of the nearest-neighbour atoms of the vacancies. This figure also defines the internal coordinate frame of the defect and we choose its origin at the position of the Si impurity. **(b)** Energy-level diagram of the SiV centre, with solid arrows denoting optical transitions. Both the electronic ground and excited state are split by spin-orbit interaction and the Jahn-Teller effect, giving the defect centre its unique four-level structure. The ground state ^2E_g is split by a frequency $\Delta E_g \sim 50\,\text{GHz}$ and the excited state ^2E_u by $\Delta E_e \sim 250\,\text{GHz}$, where the exact values depend on local strain. The four spin-doublets ($m_S \in \{\pm 1/2\}$) are further split up by the Zeeman effect when a magnetic field is applied.

The SiV centre is a point defect in diamond just like the NV centre. The structural configuration in the diamond lattice (depicted in Fig. 3(a)) is a split-vacancy aligned to the [111] axis, with the substitutional silicon atom placed bond-centred between two adjacent vacancies in the lattice.[29] The SiV's remarkable optical properties originate in part from this configuration: It belongs to the D_{3d} point group, which provides inversion symmetry and, as opposed to the NV centre, the SiV thus exhibits no permanent electric dipole moment, making it first-order insensitive to electric fields. The resulting protection of the ZPL transitions from electric field (i.e. charge) fluctuations in the environment reduces spectral diffusion and inhomogeneous broadening.[30,31] There are two observed charge states, the neutral SiV^0 and the negatively charged SiV^-, with their respective ZPLs at 946 nm[32] and 737 nm. Although the SiV^0 possesses both highly advantageous optical and spin properties, the stabilisation of this charge state is challenging, as it requires special techniques such as Fermi-level engineering of the diamond host.[32] In this thesis, we study the optical properties of SiV^- only and refer to it simply as SiV unless stated otherwise.

Fig. 4 illustrates an important difference between the optical emissions of the SiV and the NV centres: Emission is concentrated mainly into the ZPL at 737 nm, and its phonon sideband (PSB) is accordingly weak. This is

characterised by the Debye-Waller factor (i.e. the ratio between ZPL emission intensity and overall emitter emission intensity), which for the SiV centre amounts to around 75%, whereas for the NV it is only 3-4% (cf. Fig. 2(a)). As for the NV, the ZPL transition can be driven off-resonantly using a 532 nm laser, populating vibrational states, which in turn decay non-radiatively into the ^2E_u excited state.

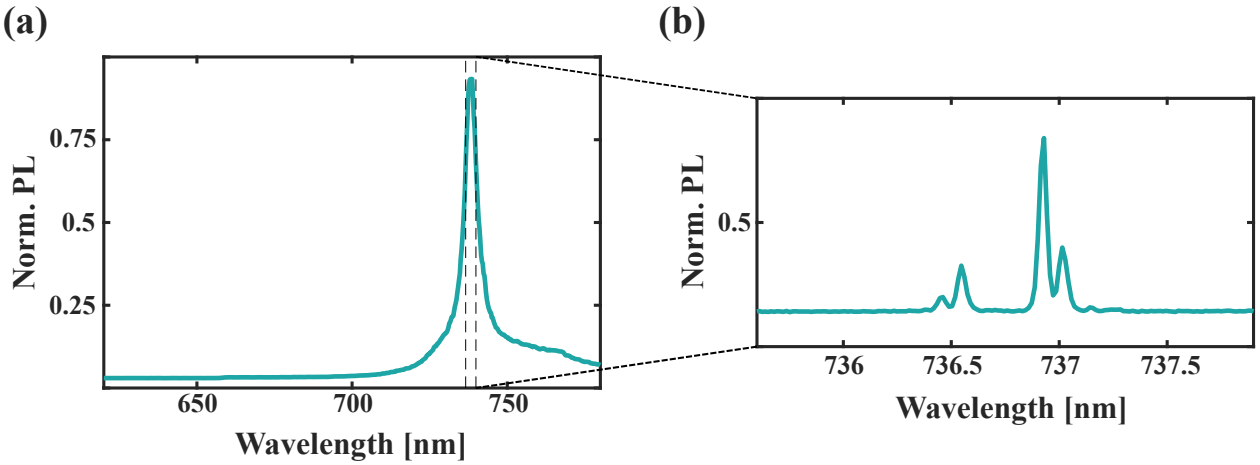

Fig. 4: **(a)** Room-temperature optical spectrum of an SiV centre with its strong ZPL line around 737 nm and comparatively weak PSB observed between 740-800 nm. **(b)** Low-temperature close-up of the ZPL of the SiV, revealing the characteristic four-line fine structure of the defect.

Ab initio calculations[33], group theory[34] or a combination of the two can be used to determine the electronic level-structure of the SiV centre, depicted in Fig. 3(b). It consist of a ^2E_g ground as well as ^2E_u and $^2A_{2u}$ excited states. The notation for these states have their origin in group theory (c.f. Appendix A): A refers to orbitally non-degenerate states while E-states are two-fold orbitally degenerate. The superscripts denote the spin degeneracy and the subscripts denote parity under inversion, g meaning even (from German: gerade) and u meaning odd (from German: ungerade). The second excited state $^2A_{2u}$ (whose additional subscript 2 denotes odd parity under 180° rotation perpendicular to the main symmetry axis [111] of the SiV) is not part of our investigation and thus omitted.

Eleven electrons determine the physics of the SiV, six originate from the dangling bonds of the nearest-neighbour carbon atoms, four from the valence shell of the silicon atom, and one from a nearby donor site, constituting its negative charge.[35] However, this model is not enough to reproduce one of the defining characteristics of the SiV centre: When cooled to liquid-helium temperatures, the ZPL transition reveals a four-line fine structure centred around 737 nm,[17] depicted in Fig. 4(b). Indeed, additional spin-orbit (SO) and Jahn-Teller (JT) interactions that lift the degeneracies of the ground and excited states explain the fine structure of the defect.[30] Additionally, in a magnetic field, each of the four states splits up further into two due to the Zeeman effect, indicating the SiV centre to be a spin-$1/2$ system with projections $m_S \in \{\pm 1/2\}$. A more detailed description given in the following section.

1.2.2 Theoretical Description and Modelling

To model the physics of the SiV centre, we follow the description given by Hepp[34] and Becker[35], where detailed derivations of the applicable Hamiltonian can be found. We consider the following interactions (omitting strain in our calculations, although it can readily be implemented using the same type of Hamiltonian as for the Jahn-Teller effect, as discussed below), describing them only briefly: Spin-Orbit, Jahn-Teller, and Zeeman. We use the basis $\{|e_{gx}\uparrow\rangle, |e_{gx}\downarrow\rangle, |e_{gy}\uparrow\rangle, |e_{gy}\downarrow\rangle\}$ for all matrix representations (for the excited state matrices, the subscript g for the basis states is replaced by u), where x and y denote the orthogonal basis functions of the two-dimensional representations $\mathrm{E_{g,u}}$ of the ground and excited state of the SiV centre. These basis states are the dangling bond symmetry adapted linear combinations (SALCs) of the SiV expanded to spin space. Their group-theoretical derivation is summarised in App. A, details can be found in the two references mentioned above.

Spin-Orbit interaction

The ground and excited states of the SiV centre are E-symmetric (i.e. two-dimensional, degenerate) states, and as such have a priori non-zero orbital angular momentum.[35] However, in the basis we have chosen, $\hat{\mathrm{L}}_x$ and $\hat{\mathrm{L}}_y$ vanish since they couple only states that are far detuned in energy (c.f. App. A),[35] and therefore the components of the orbital angular momentum operator have matrix representations (in units of $\hbar$)

$$\hat{\mathrm{L}}_x \doteq \begin{pmatrix} 0 & 0 \\ 0 & 0 \end{pmatrix} \qquad \hat{\mathrm{L}}_y \doteq \begin{pmatrix} 0 & 0 \\ 0 & 0 \end{pmatrix} \qquad \hat{\mathrm{L}}_z \doteq \begin{pmatrix} 0 & \mathrm{i} \\ -\mathrm{i} & 0 \end{pmatrix}.$$

The symmetry-adapted Hamiltonian for the ground state (g) and the excited state (e) corresponding to this interaction is then given by[30]

$$\hat{\mathrm{H}}^{\mathrm{SO}}_{\mathrm{g,e}} = \lambda_{\mathrm{g,e}} \hat{\vec{\mathrm{L}}} \cdot \hat{\vec{\mathrm{S}}} = \lambda_{\mathrm{g,e}} \hat{\mathrm{L}}_z \cdot \hat{\mathrm{S}}_z \doteq \frac{\mathrm{i}\lambda_{\mathrm{g,e}}}{2} \begin{pmatrix} 0 & 0 & 1 & 0 \\ 0 & 0 & 0 & -1 \\ -1 & 0 & 0 & 0 \\ 0 & 1 & 0 & 0 \end{pmatrix}, \tag{1.1}$$

with the orbital angular momentum operator $\hat{\vec{\mathrm{L}}} = (\hat{\mathrm{L}}_x, \hat{\mathrm{L}}_y, \hat{\mathrm{L}}_z)$, the spin angular momentum operator $\hat{\vec{\mathrm{S}}} = \hbar/2(\hat{\sigma}_x, \hat{\sigma}_y, \hat{\sigma}_z)$, where $\hat{\sigma}_k, k \in \{x, y, z\}$ are the Pauli matrices, and the coupling constant $\lambda_{\mathrm{g,e}}$; the subscripts indicate the ground or the excited state respectively. For the present discussion we have chosen the basis of dangling bond SALCs of the SiV for reasons of simplicity and symmetry, but note that the SALCs are not eigenstates of $\hat{\mathrm{L}}_z$. The matrix representation of $\hat{\mathrm{H}}^{\mathrm{SO}}_{\mathrm{g,e}}$ is therefore not diagonal. Still, we remark that simple linear combinations of the SALCs (c.f. App, A) produce eigenstates of $\hat{\mathrm{L}}_z$, diagonalising the matrix representation of $\hat{\mathrm{H}}^{\mathrm{SO}}_{\mathrm{g,e}}$. Additional information can also be found in Hepp et al.[30]

Jahn-Teller interaction

The second interaction that lifts the orbital degeneracies of the ^{2}E-states is the Jahn-Teller effect. The Jahn-Teller theorem states that partially filled states of a non-linear molecular system that are orbitally degenerate are unstable. The system therefore seeks to lift the degeneracy by lowering its symmetry, undergoing a geometrical distortion.[36]

Indeed, this is the case for both the ground and the excited state of the SiV. A purely orbital effect, the corresponding Hamiltonian must additionally be expanded to spin-space (in contrast to Eq. (1.1)) by a direct product with the 2×2 identity matrix, and is thus given by

$$\hat{\mathrm{H}}^{\mathrm{JT}}_{\mathrm{g,e}} \doteq \begin{pmatrix} \Upsilon_{x,\mathrm{g,e}} & \Upsilon_{y,\mathrm{g,e}} \\ \Upsilon_{y,\mathrm{g,e}} & -\Upsilon_{x,\mathrm{g,e}} \end{pmatrix} \otimes \begin{pmatrix} 1 & 0 \\ 0 & 1 \end{pmatrix}$$

$$\doteq \begin{pmatrix} \Upsilon_{x,\mathrm{g,e}} & 0 & \Upsilon_{y,\mathrm{g,e}} & 0 \\ 0 & \Upsilon_{x,\mathrm{g,e}} & 0 & \Upsilon_{y,\mathrm{g,e}} \\ \Upsilon_{y,\mathrm{g,e}} & 0 & -\Upsilon_{x,\mathrm{g,e}} & 0 \\ 0 & \Upsilon_{y,\mathrm{g,e}} & 0 & -\Upsilon_{x,\mathrm{g,e}} \end{pmatrix}. \tag{1.2}$$

It remains to be noted that any other purely orbital interaction as well as potential crystal strain acts on the electronic states of the SiV the same way the JT effect does. Joint effects of different interactions are hence obscured and cannot easily be distinguished.[35]

Zeeman interaction

In a static magnetic field, the spin degeneracy of the SiV is lifted by the Zeeman effect, enabling optical access to the individual spin-states of the defect. The symmetry-adapted Hamiltonian takes the form

$$\hat{\mathrm{H}}^{\mathrm{Z}}_{\mathrm{g,e}} = q\gamma_L \hat{\vec{\mathrm{L}}} \cdot \vec{B} + \gamma_S \hat{\vec{\mathrm{S}}} \cdot \vec{B}$$

$$\doteq q\gamma_L \begin{pmatrix} 0 & 0 & \mathrm{i}B_z & 0 \\ 0 & 0 & 0 & \mathrm{i}B_z \\ -\mathrm{i}B_z & 0 & 0 & 0 \\ 0 & -\mathrm{i}B_z & 0 & 0 \end{pmatrix}$$

$$+ \frac{\gamma_S}{2} \begin{pmatrix} B_z & (B_x - \mathrm{i}B_y) & 0 & 0 \\ (B_x + \mathrm{i}B_y) & -B_z & 0 & 0 \\ 0 & 0 & B_z & (B_x - \mathrm{i}B_y) \\ 0 & 0 & (B_x + \mathrm{i}B_y) & -B_z \end{pmatrix}, \tag{1.3}$$

with the first term representing the orbital contribution and the second the spin contribution. $\hat{\vec{\mathrm{L}}}$ is the orbital angular momentum operator, $\hat{\vec{\mathrm{S}}}$ the spin angular momentum operator (both defined as before for the SO interaction), and $\vec{B} = (B_x, B_y, B_z)$ the magnetic field in the internal reference frame of the SiV, defined in Fig. 3(a). $\gamma_L = \mu_B/\hbar$ and $\gamma_S = 2\mu_B/\hbar$ are the orbital and electron gyromagnetic ratios. Following experimental evidence, a quenching factor q acting on the orbital part of $\hat{\mathrm{H}}^{\mathrm{Z}}_{\mathrm{g,e}}$ of the order of 0.1 is introduced to account for orbital quenching (i.e. a reduction of orbital contributions to the dynamics of the system[37]) in the presence of JT interaction.[30] We note that since $\hat{\mathrm{L}}_x$ and $\hat{\mathrm{L}}_y$ vanish as discussed before, B_x and B_y do not contribute to the orbital part of the Hamiltonian.

It is useful to convert this Cartesian form of the magnetic field $\vec{B}$ to spherical coordinates. The problem then simplifies from three Cartesian coordinates (B_x, B_y, B_z) to two spherical coordinates ($\|B\|$, θ), where θ denotes the relative angle between the quantisation axis of the SiV (the high-symmetry, or z-axis) and the direction of the magnetic field. From numerical calculations we note that varying the azimuthal angle ϕ of the magnetic field does not affect the electronic level structure (cf. App. B). We set this angle to the arbitrary value of 45°. This facilitates calculations and directional considerations of the magnetic field, determining the change in energy as a function of the magnitude $\|B\|$.

We can now model the electronic states of the SiV centre by diagonalising the full Hamiltonian

$$\hat{\mathrm{H}}_{\mathrm{g,e}} = \hat{\mathrm{H}}^{\mathrm{SO}}_{\mathrm{g,e}} + \hat{\mathrm{H}}^{\mathrm{JT}}_{\mathrm{g,e}} + \hat{\mathrm{H}}^{\mathrm{Z}}_{\mathrm{g,e}}. \tag{1.4}$$

Solving the Schrödinger equation $\hat{\mathrm{H}}\psi = E\psi$ for the Hamiltonian (1.4) yields the eigenstates ψ of the system as well as the eigenenergies, E. From this, we can easily calculate the optical transition frequencies between the ground and excited state manifold, given by $\omega_j = \frac{1}{\hbar}(E_i - E_f)$, where j denotes the optical transition between the excited state with energy E_i and the ground state with energy E_f. To complete the picture, selection rules and transitions strengths will be discussed further below. The results of these calculations are depicted in Fig. 6(a), (b) and (c) for different magnetic field strengths and a relative angle of 54.7° between the magnetic field and the symmetry axis of the SiV. This angle corresponds to the experimentally most readily implemented situation that a magnet is placed directly under the [100] sample, the magnetic field aligned along the z-axis of the lab-frame.

At this point it is worth defining a nomenclature to identify the optical transitions of the SiV. In zero field, there are four possible optical transitions, which are usually denoted A, B, C, and D (cf. Fig. 5).
When a magnetic field is applied to the defect, each of the four levels splits up into two more levels. This results in additional possible transitions (including optical non-spin-conserving transitions if the field is off-axis to the defect). In that case, the nomenclature for the transitions is, according to the literature standard, labelled corresponding to the levels involved. The ground state levels are denoted $|1\rangle, ..., |4\rangle$ and the excited state levels are denoted $|\mathrm{A}\rangle, ..., |\mathrm{D}\rangle$, both ordered according to ascending energy. An optical transition between excited state $|\mathrm{A}\rangle$ and ground state $|3\rangle$ is then denoted as A3. Both zero-field transitions and transitions that occur when an off-axis field is applied are illustrated in Fig. 5(a), and a normalised optical spectrum of the SiV (recorded at low-temperature and at zero-field) with the corresponding labels is shown in Fig. 5(b).
In the zero-field limit, the fine structure is determined by SO and JT interactions, and the splitting between the two ground and the two excited states is given by

$$\Delta E_{\mathrm{g,e}} = \sqrt{\lambda^2_{\mathrm{g,e}} + 4\Upsilon^2_{\mathrm{g,e}}}, \tag{1.5}$$

where $\Upsilon^2_{\mathrm{g,e}} = \Upsilon^2_{x,\mathrm{g,e}} + \Upsilon^2_{y,\mathrm{g,e}}$ is the total JT contribution to the zero-field splitting.

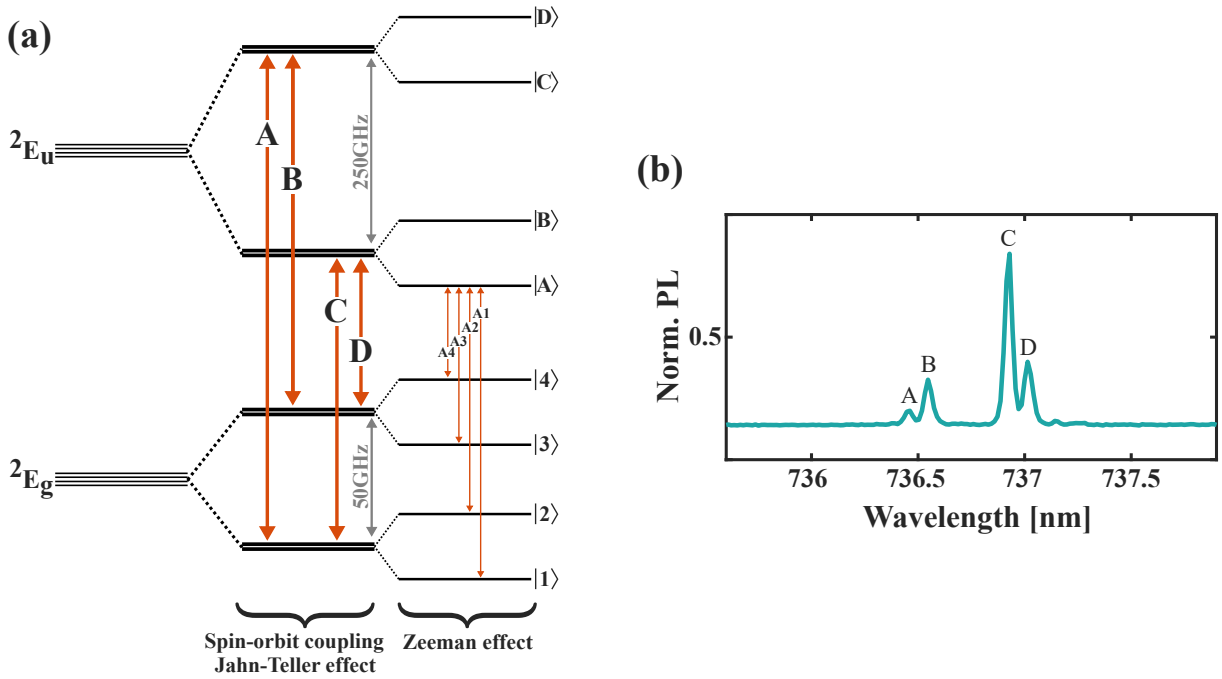

Fig. 5: **(a)** Level structure of the SiV centre, including the three interactions discussed in the main text: spin-orbit interaction, Jahn-Teller effect, and Zeeman effect. At zero-field, the four optical transitions that result from the SiV's fine-structure are denoted with the letters A, B, C, and D. The same labels are applied to the experimental low-temperature, optical spectrum in **(b)**, which was already introduced in fig. 4 (cf. also Sect. 3.2.2 for further experimental details). When a magnetic field is applied to the defect, the spin doublets are further split up into a total of eight states, which are named $|1\rangle, ..., |4\rangle$ in the ground state and $|A\rangle, ..., |D\rangle$ in the excited state. The transition between two levels is then indicated by the alphanumerical doublet corresponding to these particular states. For example, the transition $|A\rangle \longleftrightarrow |3\rangle$ is denoted A3.

Optical transition strengths

In order to calculate transition strengths, we consider the dipole operator $\hat{p} = -e \cdot \hat{r}$ where e is the electron charge and $\hat{r}$ is the position operator. In a D_{3d}-symmetric system (cf. App. A), its components can be written as[35]

$$\hat{p}_x \sim \begin{pmatrix} 1 & 0 \\ 0 & -1 \end{pmatrix} \qquad \hat{p}_y \sim \begin{pmatrix} 0 & -1 \\ -1 & 0 \end{pmatrix} \qquad \hat{p}_z \sim \begin{pmatrix} 1 & 0 \\ 0 & 1 \end{pmatrix}. \tag{1.6}$$

These representations of the components of the dipole operator must be expanded to spin space by using the appropriate direct product, exactly as for $\hat{H}^{JT}_{g,e}$. We can then calculate the intensities associated with each optical transition by calculating the matrix elements of the dipole operator between the eigenstates of $\hat{H}_{g,e}$, always linking an excited state and a ground state. That is, we calculate the intensity I_j of each optical transition j by calculating the dipole-matrix element between a state ψ_i from the excited-state manifold and a state ψ_f from the ground-state manifold linked by said transition.

In our experiments, we perform unpolarised PL detection. Hence, we sum up the contributions from each of the three components of the dipole operator, weighted with their respective collection efficiency η_k, $k \in \{x, y, z\}$ (which can be calculated numerically but are set to unity for the present discussion). η_k are determined by the

dipolar characteristics of each transition and depend on the oscillation direction of the emitted fields. This yields the overall intensity

$$I_j = n_i(T)\left(\eta_x \left|\langle\psi_f|\,\hat{\mathrm{p}}_x\,|\psi_i\rangle\right|^2 + \eta_y \left|\langle\psi_f|\,\hat{\mathrm{p}}_y\,|\psi_i\rangle\right|^2 + \eta_z \left|\langle\psi_f|\,\hat{\mathrm{p}}_z\,|\psi_i\rangle\right|^2\right). \tag{1.7}$$

$n_i(T)$ is a thermal weighing factor between the excited states, which has to be taken into account since the thermalisation timescales are much smaller than the excited state lifetimes.[38] Changing the temperature of the diamond lattice leads to a change in relative peak heights of the transitions in the optical spectrum, since the relative intensity of an optical transition is related to the occupation n_i of the initial state. $n_i(T)$, is then the occupation probability of excited state i, given by the Boltzmann distribution

$$n_i(T) = n_A \exp\left(-\frac{E_i - E_A}{k_\mathrm{B} T}\right), \tag{1.8}$$

where n_A is the population of the lowest energy excited state with energy E_A, E_i is the energy of state i, T is the diamond lattice temperature and k_B the Boltzmann constant. For additional information on the temperature response of the SiV see App. C.

For the sake of simplicity and according to previous work by Hepp,[34] we model each optical transition j by a Lorentzian

$$L_j(\omega) = \frac{I_j \cdot \gamma^2}{\gamma^2 + (\omega - \omega_j)^2}, \tag{1.9}$$

centred at the transition frequency ω_j and with full width at half maximum (FWHM) $2\gamma = 0.14\,\mathrm{nm}$, corresponding to the resolution of the spectrometer that we use to record experimental spectra.

With this, we are now able to fit the fine structure spectrum of the SiV. The resulting fit parameters can be found in Tab. 1. Using these values and the model presented above, we can describe and predict the anticipated optical spectra of the SiV centre, including the effect of an arbitrarily aligned magnetic field. Exemplary results of this calculation are depicted in Fig. 6(a)-(d), showing the level structure (a) and (b) and the optical transition frequencies with transition strengths (c) as a function of magnetic field strength (at an angle of 54.7° from the SiV high-symmetry axis in a [100] sample, i.e. aligned along the z-axis of the lab-frame), and a zero-field fine structure spectrum (d), reproducing the four characteristic lines and achieving good agreement with experimental data.

λ_g [GHz]	λ_e [GHz]	Υ_g [GHz]	Υ_e [GHz]	q	T [K]	2γ [nm]
47	257	8	16	0.1	8.5	0.14

Tab. 1: Fit parameters for the SO coupling constants and the JT coupling constants (assuming $\Upsilon_{\mathrm{g,e},x} = \Upsilon_{\mathrm{g,e},y}$), defining the zero-field splitting between ground and excited states. Additionally, the quenching factor q, the diamond lattice temperature T, and the FWHM 2γ is also listed to complete the free parameters of the calculation. Data for the fitting were recorded during our experiments (c.f. Sect. 3.2.2).

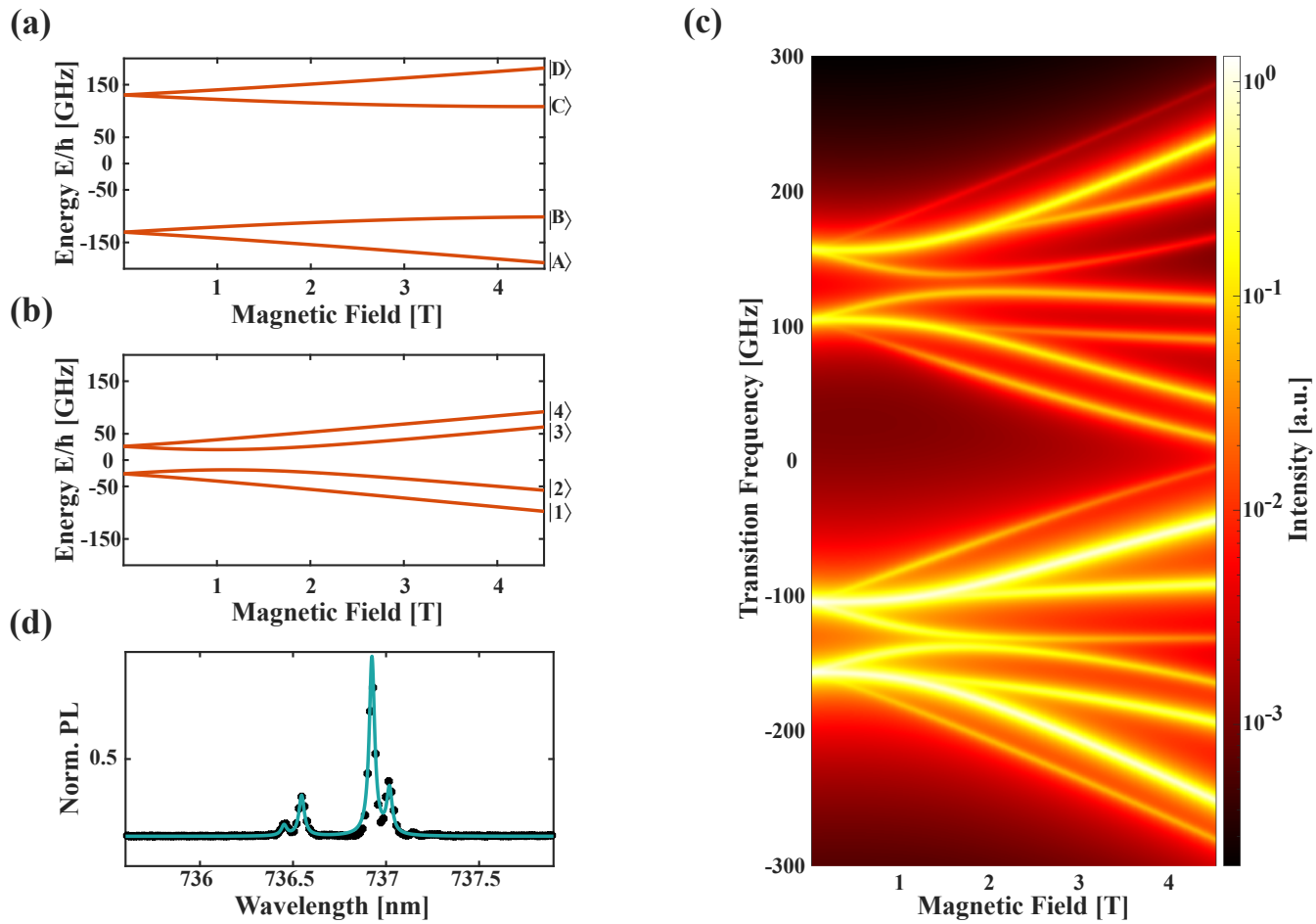

Fig. 6: **(a)** Excited state level structure calculated with the model introduced in this chapter as a function of the magnetic field at an angle of 54.7° to the symmetry axis of the SiV in a [100] sample, corresponding to a magnetic field aligned to the z-axis of the lab-frame. The corresponding states are marked to the right. **(b)** Ground state level structure calculated from the model under the same conditions as in (a). Avoided crossings stemming from the SO interaction appear around 2 T. The corresponding states are marked to the right. **(c)** Optical transition frequencies calculated from the level energies as a function of the magnetic field at the same angle as in (a) and (b). The colour map shows transition strength. These data can be used to gauge which magnetic field is suitable to optically address particular spin-states within one transition. **(d)** Experimental zero-field optical spectrum in black dots and corresponding fit shown in mint. The relative heights of the peaks correspond to a sample temperature of 8.5 K, slightly higher than the temperature measured in the cryostat of 6.8 K.

In summary, this chapter introduced both the NV centre and the SiV centre and their respective physical properties. The spin polarisation mechanism of the NV and its application in magnetometry and quantum information processing is explained and the basic physics of the SiV is discussed in depth, outlining a model to describe the electronic states and the optical transitions of the defect. We will now move on to Chap. 2 and introduce the samples and the setup that were used in the experiments, which are outlined in Chap. 3.

Chapter 2

Setup and Samples

This chapter briefly introduces the low-temperature confocal microscopy setup (Sect. 2.1) and the samples (Sect. 2.2) that were used to perform the experiments.

2.1 Setups

For both the NV and the SiV experiments, we use two different, home-built confocal optical microscopy setups, schematics of which are depicted in Fig. 7. While the setups are different, we use the same optical-table cryostat (attoDRY800) for both experiments, featuring a base-temperature of 6 K. Both setups feature in principle the same components, the only difference being the excitation and detection wavelengths they are optimised for (NV-ZPL: 637 nm, SiV-ZPL: 737 nm).

The NV setup consists of a Cobolt 515 nm laser (06-MLD) used to excite the NV off-resonantly and a tunable New Focus diode laser with wavelengths ranging from 636 nm to 639 nm (TLB-6700). Both lasers are controlled with a separate acousto-optical modulator (AOM, Crystal Technology Inc. 3200-146 and Gooch & Housego R15210) to enable power adjustments and, more importantly, pulsed excitation. The green and the red lasers are guided to the objective (Olympus, 100x, NA = 0.9) by a 560 nm dichroic filter (Semrock FF560) and a 635 nm dichroic filter (Semrock R635), respectively. The 635 nm filter also allows the collected NV fluorescence to be passed to an APD (Excelitas SPCM), in front of which a pinhole is placed in order to achieve confocal microscopy. There is a second detection arm leading to a spectrometer (Princeton Instruments SP-2500), used to measure the zero-phonon line (ZPL) wavelength of the investigated NV.

The SiV-setup uses a PicoLAS 532 nm laser (LDP-V 03-100 UF3) and a tunable New Focus diode laser (TLB-6700, tuning range 730 nm to 739 nm) for off-resonant and resonant excitation respectively. For this setup, only the red laser is equipped with an AOM (Gooch & Housego R15210). As for the NV-setup, two dichroic filters (Semrock FF740 and R635) guide the red and the green laser to the objective in the vacuum shroud of the cryostat. The 740 nm dichroic separates the PSB-collection arm from the excitation arm, and an additional 90:10 beamsplitter guides light from the sample to the ZPL-collection arm. Additionally, a 750 nm long-pass (LP) filter (Thorlabs FELH0750) is placed in front of the PSB-collection fiber-coupler to clean up any back-reflection of the resonant red laser.

For both setups, a fiber beam splitter siphons off a portion of the resonant laser and guides it to a wavelength meter (HighFinesse WS-U) that is used to stabilise the wavelength of the laser for the resonant-excitation experiments (photoluminescence excitation (PLE)). A HeNe-laser at 632 nm placed on the table is used for calibration of the wavelength meter. This enables wavelength stabilisation for the two resonant lasers through a PID loop, lest they drift out of resonance with the defect centre under investigation.

The vacuum shroud of the cryostat houses piezo steppers (Attocube ANPx101/LT and ANPz102/LT) for rough positioning of the sample and xyz-piezo scanners (Attocube ANSxyz100/LT) for confocal scans. Microwaves are generated by a SRS SG384 and delivered to the sample by a microwave feedthrough to enable driving of the NV ground-state spin-levels.

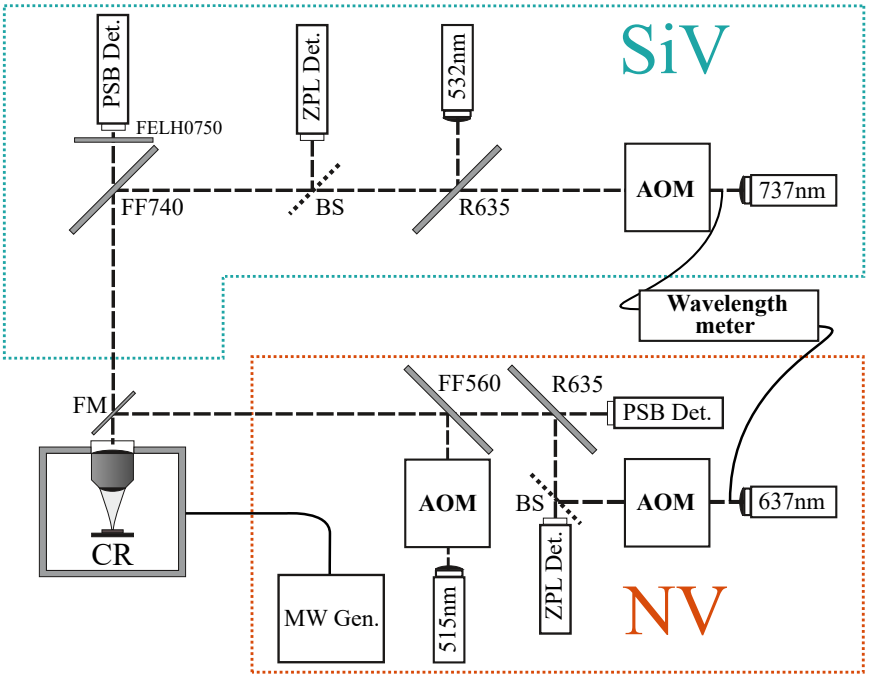

Fig. 7: Schematic of the SiV and the NV setup. Details like mirrors, lenses, and pinholes are mostly omitted for clarity. The cryostat is denoted CR and a flip mirror separating the two setups is denoted FM.

2.2 Samples

NV Sample #1

The first sample is an electronic-grade single-crystal diamond provided by Element Six and polished by Almax. Its natural nitrogen concentration is <5ppb and its boron concentration <1ppb. Three locations on this sample were investigated: A large bulk area, a membrane with a thickness of ~2 µm and an area with nano-structured diamond cantilevers. Scanning electron microscope (SEM) images of the sample are displayed in figure 8(a). The fabrication of both samples used in our experiments is not part of this investigation and documented elsewhere.[39,40] After nano-structuring, the sample was implanted by the company CuttingEdgeIons with ^{15}N ions at 12 keV and 1×10^{11} ions/cm^2, where the scarcely occuring (0.4 % natural abundance) ^{15}N isotope was selected to later identify the source (pre-existing in the diamond or implanted) of the investigated NV centres. After im-

plantation, we annealed the sample in a vacuum-annealing oven. This process creates NV centres from both the implanted ^{15}N and the inherent ^{14}N atoms. The post-fabrication implantation employed here contrasts the usual process of creating NV centres, where nitrogen implantation is performed as the first step and nano-structuring as the second.[39] It was one of the key questions and hypotheses of this thesis whether such post-implanted NV centres could yield better (optical) coherence properties than those created in the usually employed way.

SiV Sample #2

This sample is also is an electronic-grade diamond provided by Element Six and polished by Almax. Before nano-fabrication and annealing, the sample was implanted by the company Innovion with ^{28}Si ions at 80 keV and a density of 1.5×10^{11} ions/cm^2. Subsequently, we annealed the sample for four hours at 400 °C, for eleven hours at 800 °C and, finally, for two hours at 1300 °C. After the bake-out step at 400 °C, actual SiV formation takes place in the second step at 800 °C, when vacancies become mobile. The final annealing step is expected to remove lattice damage and other impurities.[15,41] After confirming that the annealing of the sample created SiV centres, we nano-structured the sample and created a 5×5-grid of nano-pillar fields (cf. SEM images in figure 8(b)). After characterising the sample, a second annealing procedure with the same recipe as before nano-structuring was carried out to once more heal damage introduced during processing of the sample.

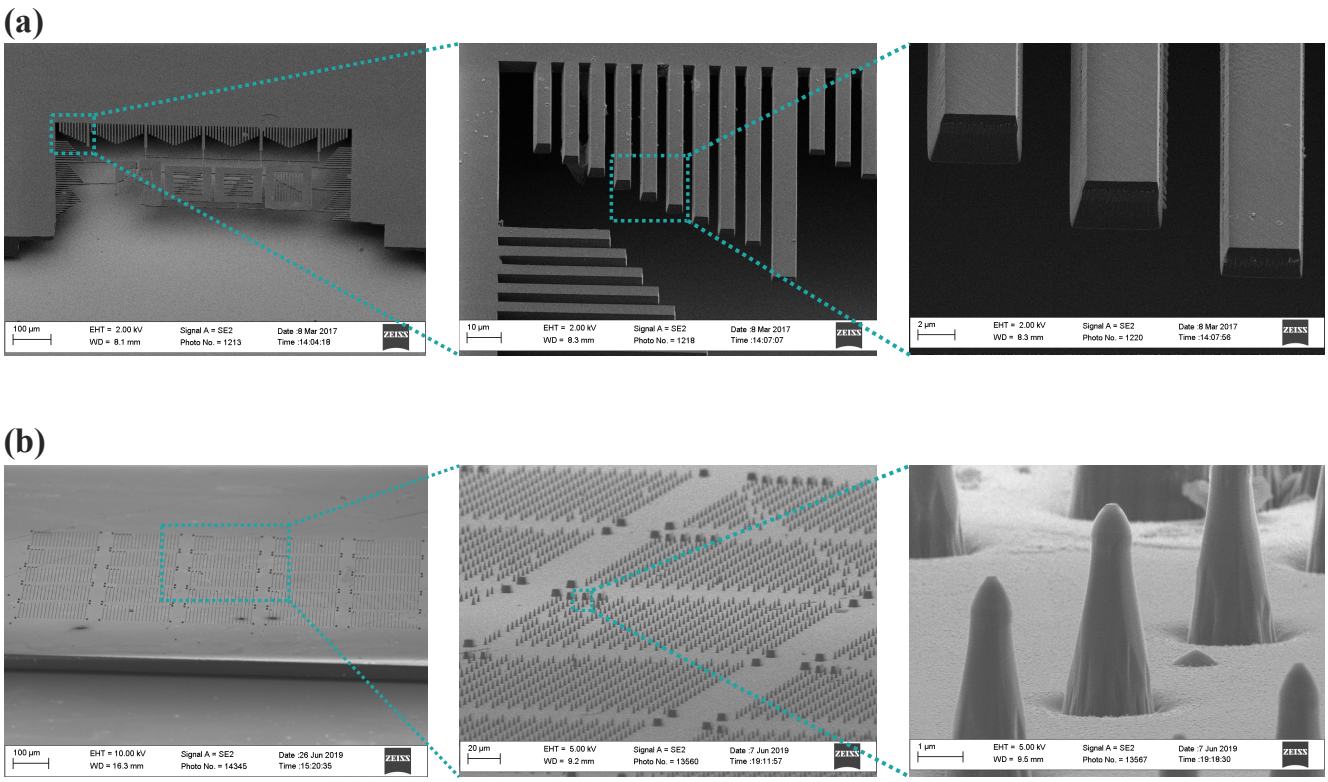

Fig. 8: **(a)** SEM images of NV Sample #1. Successive close-ups are marked in mint. On the first image, all of the structured parts (membrane and cantilevers) of the sample are visible. The first close-up depicts part of a cantilever family, and the second depicts three of the cantilevers individually. **(b)** SEM images of SiV sample #2. The first image shows all 25 pillar-fields, a close-up of one of which is depicted in the second image. The third image shows a close-up of a few selected pillars.

Chapter 3

Experiments and Results

This chapter concerns the main experiments that were conducted within this thesis. In Sect. 3.1, isotopic labelling of NV centre optical coherence is treated by introducing the methodology involved and presenting the results. Subsequently, we characterise the optical properties of SiV centres at both room temperature and 4 K in Sect. 3.2.

3.1 NV Isotopic Labelling of Optical Coherence in Nano-Structures

The methodology of this experiment is closely linked to its motivation. As laid out in the introduction to this thesis, the spin-properties of the NV centre are excellent; its spin is optically addressable with long spin-coherence times approaching one second,[42] making it a promising candidate for quantum information protocols.[3] The shortcomings in its optical properties such as long radiative lifetimes, low Debye-Waller factor (i.e. the ratio of the intensity of emission of the zero-phonon line (ZPL) and overall intensity of emission of the defect), low coherent-photon extraction efficiency, and strong random spectral diffusion, however, prevent its use as a scalable solid-state qubit platform. In principle, the first three issues can be addressed (while preserving its outstanding spin-coherence) by coupling the NV centre to a high-quality optical micro-cavity, which has recently been demonstrated.[10] However, while incorporating the NV centre into the cavity does address its mediocre optical properties, the nano-structuring necessary to do so introduces a new challenge: The optical coherence of the photons emitted at the zero-phonon line (ZPL) of the NV centre is diminished after processing bulk diamond into thin membranes of $\sim$2 µm thickness, which is required for incorporation into the cavity. Specifically, the NV centre's optical linewidth typically increases from $\sim$100 MHz in bulk to over 1 GHz in the nano-structured samples.[43] This broadening of the line possibly originates from the process of ion-implantation (widely used to create NV centres). Ion-implantation is an invasive process that introduces damage to the diamond-lattice, which supposedly worsens in the subsequent nano-fabrication. As a result, the optical coherence of the NV deteriorates.

There are several possibilities to continue on the path towards a NV spin-photon qubit interface. First, one can try to find other ways of creating NV centres in diamond. Laser writing of the defect is a possibility, where the damage caused to the lattice is contained to the focal volume of the laser, which possibly increases chances of creating highly coherent NV centres.[44] Another possibility is to optimise the mechanism of ion-implantation and investigate its detrimental role to optical coherence of the NV centre further. One approach could be implantation of nitrogen ions only after nano-structuring is completed. This route is followed in this thesis and its implementation is the subject of the next section.

3.1.1 Methodology

We performed our experiment on isotopic labelling of NV optical coherence on sample #1. As mentioned in Sect. 2.2, this sample was implanted with ^{15}N ions after nano-structuring, and subsequently annealed to create NV centres. NV centres are formed both from the naturally abundant ^{14}N isotope and the implanted ^{15}N isotope. While the two cannot be easily distinguished from their spectral properties alone, it is possible to identify the two classes according to the different nuclear spins of the isotopes, where ^{15}N exhibits an $I = 1/2$ and ^{14}N an $I = 1$ nuclear spin. This difference manifests itself, for example, in pulsed optically detected magnetic resonancen (pODMR) measurements (cf. Sect. 1.1.1) where the hyperfine structure of the NV in question can be resolved. For ^{15}N the ODMR hyperfine structure consists of two dips separated by 3.1 MHz, corresponding to the transitions $|m_S = 0, m_I = 0\rangle \longleftrightarrow |\pm 1, \pm 1/2\rangle$ while for ^{14}N, there are three dips separated by 2.1 MHz, matching the transitions between $|0, 0\rangle$ and $|\pm 1, \pm 1\rangle$, and $|0, 0\rangle$ and $|\pm 1, 0\rangle$ (see also Fig. 9(b) and (d) for typical pulsed ODMR spectra).[45] Building on this, we can isotopically label NV centres and distinguish between defects formed from 'natural' (i.e. not implanted) ^{14}N and implanted ^{15}N. We note that ^{15}N can also be naturally present in the diamond lattice, and thus not all ^{15}NV centres that we find must necessarily originate from implanted nitrogen. However, since ^{15}N is so scarcely occurring (natural abundance: 0.4%), we neglect this possibility.

Accordingly, the goal of this experiment is to investigate the optical coherence of NV centres by measuring their linewidths and determining if they were formed from implanted ^{15}N or from naturally occurring ^{14}N. To this end, we probe a number of NV centres in different parts of the sample (bulk and nano-structured) and statistically analyse the resulting dataset.

In our study, we begin by confocally scanning an area of the sample to identify potential NV centres. We then record an optical spectrum at each bright spot, to determine whether it is in fact an NV centre. If it shows the characteristic ZPL near 637 nm in its spectrum, then we classify it as an NV and investigate it further. Next, we scan the wavelength of the tunable red diode laser across the ZPL position of the candidate to perform a resonant photoluminescence excitation (PLE) measurement. The PLE is measured by collecting the phonon sideband (PSB) emission with an APD while the laser wavelength is swept across the transition, with a rise in counts indicating that the laser is resonant with the ZPL. The laser wavelength is monitored by a wavelength meter and actively stabilised by a PID feedback loop.
We also determine which isotope of nitrogen the NV centre has by performing a pulsed ODMR measurement. To determine the $|m_S = 0\rangle \longleftrightarrow |m_S = \pm 1\rangle$ transition frequency of the ground state spin, we sweep the microwave (MW) frequency across the transition and measure the fluorescence count rate. Once we identify the transition frequency, we set our MW generator to it and apply MW pulses of different durations to the NV. By sweeping the pulse duration, we can observe Rabi oscillations and thereby identify the π-pulse time (i.e. the time it takes to coherently transfer all of the spin population from the $|m_S = 0\rangle$ state to the $|m_S = \pm 1\rangle$ state). After finding the π-pulse time, we can perform a pulsed ODMR measurement (cf. Fig. 9(b) for the pulse sequence). As the pulsed ODMR measurement eliminates power broadening from the MW fields,[46] we are able to resolve the hyperfine structure of the NV centre and thereby identify the isotope of the nitrogen atom. We repeat the combination of PLE to measure the linewidth and pulsed ODMR to determine the isotope for each NV centre. The set of these measurements then comprises our linewidth dataset.

3.1.2 Results

In total, we obtained data from 51 NV centres from all three sample areas: bulk, membrane, and cantilevers. In our statistics, we grouped membrane and cantilever NV centres together since they share comparable behaviour. Fig. 9(a) shows typical PLE data in bulk with a narrow FWHM linewidth of 112 MHz as determined from a Gaussian fit (depicted in red) for one of the peaks and a linewidth of 310 MHz for the other. Two peaks in the PLE data can either arise from strain splitting of the ^{3}E level at low temperature into two branches, denoted ^3E_x and ^3E_y,[3] or from two NV centres close to each other that emit at almost the same wavelength. For the former case, as it is a single NV with two transitions, it is in general expected that both peaks exhibit very similar linewidths, which need not be the case for two separate NVs in close spectral and spatial vicinity. For the case depicted in Fig. 9(a), we observe a significant difference in linewidth, pointing towards the case of two different NV centres. The difference in linewidths could also be explained by the fact that the red excitation laser's polarisation is not well defined in this experiment, and it is therefore possible that one of the two transitions arising from strain splitting in a single NV is addressed more effectively than the other (since they are polarised orthogonally). This can lead to power broadening. Indeed, the difference between the Gaussian fit and the data supports this interpretation as well. For most of our NV centres, only one branch is visible within our usual scan-range of 10-20 GHz, implying high strain in the sample.

The pODMR measurement corresponding to the PLE data in Fig. 9(a) is depicted in Fig. 9(b), showing three dips in the hyperfine spectrum, separated by 2.1 MHz, which clearly identify the NV's isotope as ^{14}N. Fig. 9(c) shows PLE data of a broad-linewidth (Gaussian FWHM ∼3.2 GHz) NV in bulk, and in Fig. 9(c), the pODMR reveals a two-dip hyperfine structure, with lines split by 3 MHz, assigning this NV to ^{15}N. Note that the spin resonances for the data in Fig. 9(b) and (d) are different due to slightly different placements of external magnets in the two cases. Such bias magnetic fields were applied in order to lift the degeneracy of the $|m_S = \pm 1\rangle$ states to obtain more clearly resolvable pODMR hyperfine spectra. The pulse sequences we use for the photoluminescence excitation (PLE) consist of a green initialisation pulse and then excitation and readout with the red laser, as depicted in the schematic above Fig. 9(a). For pODMR, we initialise with a green laser pulse, subsequently drive the spin with a MW π-pulse and then perform a spin-readout pulse with the green laser. The pulse sequence is shown in the schematic above Fig. 9(b).

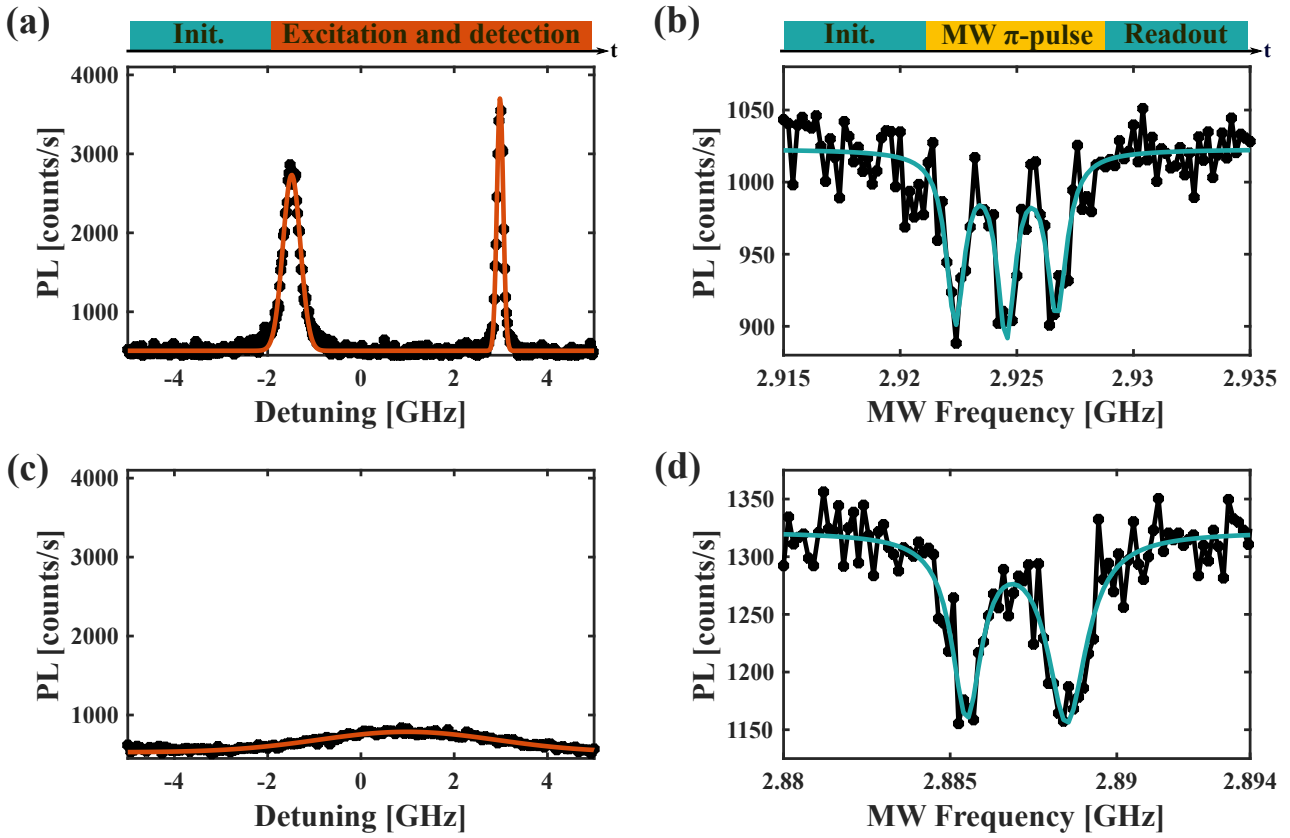

Fig. 9: **(a)** Typical PLE data for an NV obtained in bulk with a pulse sequence as illustrated on top of the panel. Gaussian fits (orange) to the data (black dots) reveal a FWHM linewidth of 310 MHz for the left peak and 112 MHz for the peak to the right. This significant difference in linewidth indicates that we probe two different NV centres close to each other (see main text). **(b)** Pulsed ODMR of the same NV centre as in (a), measured with a pulse-sequence as depicted above the panel. The data reveals the NVs hyperfine structure and shows three dips separated by 2.1 MHz, identifying the isotope to be ^{14}N. **(c)** Resonant Excitation data for another NV in bulk plotted on the same scale as in (a). Gaussian fitting determines a FWHM linewidth of 3.2 GHz. **(d)** Pulsed ODMR of the same NV as in (c). Fitting the data determines the hyperfine-separation of the two dips to be 3 MHz, identifying the isotope to be ^{15}N.

A summary of our findings from all 51 investigated NV centres is depicted in Fig. 10. For all figures, we show quantities as a function of the FWHM linewidth of one of the two possible branches, arbitrarily choosing E_x, since we cannot deduce which of the branches we observe from our data.

Fig. 10(a) depicts the spread in ZPL wavelength as a function of the measured linewidth, which, except for three ^{15}NV centres in bulk, lie within a range between 636.8-637.2 nm, indicating relatively uniform strain across the sample.[47] This observation indicates that linewidths are not affected by static strain, which is further supported by the data in Fig. 10(b), where the splitting between E_x and E_y is plotted against the E_x linewidth (for those cases where a splitting could be observed). For all NV centres for which both peaks were observed, the peak splitting was 1.5-10 GHz, again suggesting that static strain does not affect the optical coherence of these NV centres.

Fig. 10(b) shows a histogram of the acquired data, resolved by location on the sample. We observe two distinct distributions, one representing narrow linewidth (mean FWHM value of 0.3 GHz) and the other broader linewidth (mean FWHM value of 15 GHz) NV centres. Interestingly, both distributions incorporate NV centres from bulk and the nano-structured part of the sample, indicating that for post-fabrication implanted NV centres, optical coherence is not affected by sample-structuring (at least down to the membrane size of ~2 µm).

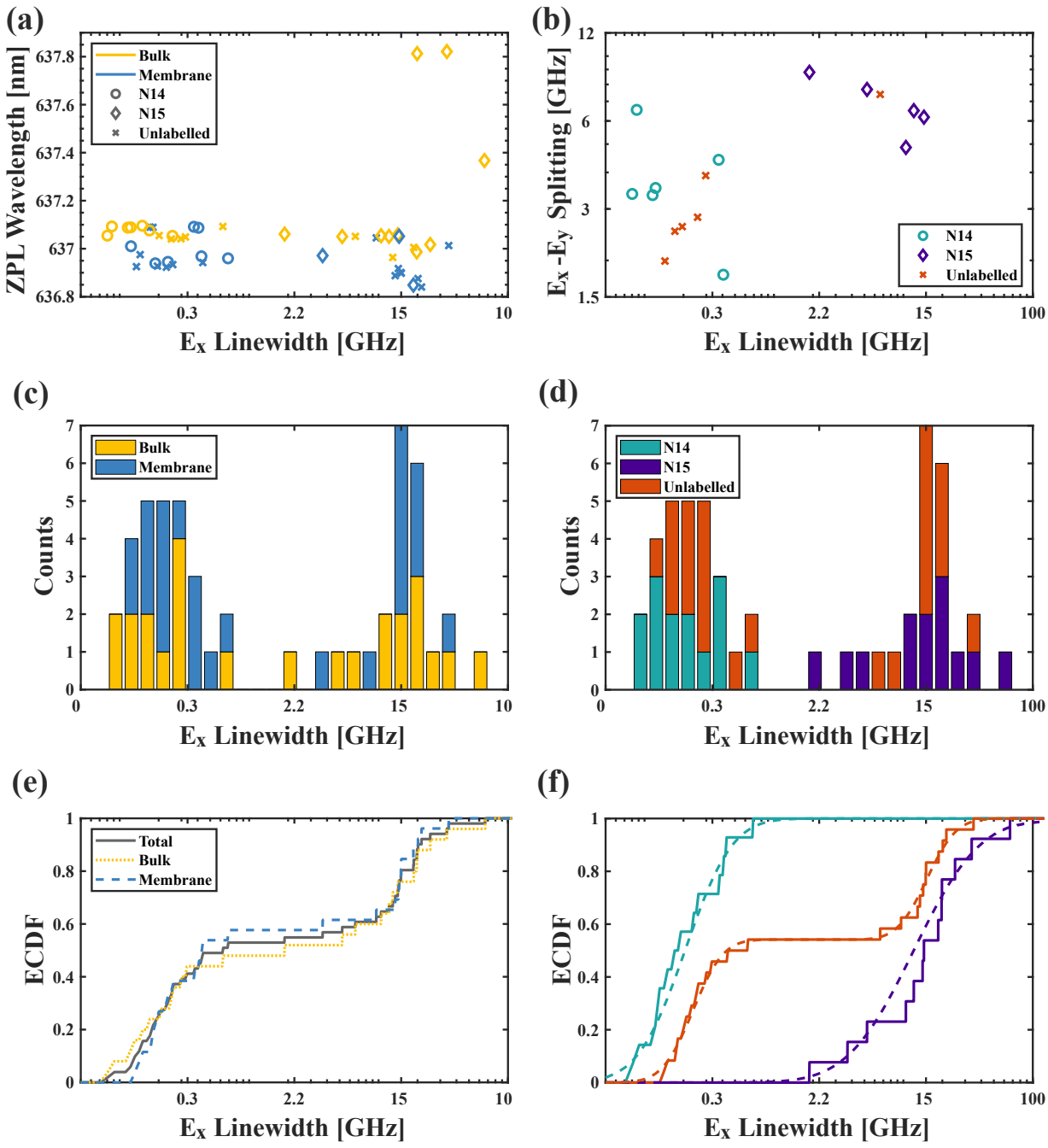

Fig. 10: **(a)** ZPL position as a function of linewidth of the NV centres in our dataset, grouped by location. Since all but three of the centres are within a range of 636.8-637.2 nm, we conclude that strain in the sample is distributed evenly and does not seem to affect optical coherence. **(b)** Separation of E_x and E_y as a function of E_x linewidth. If two peaks were detected in PLE, their separation is a measure of the local strain environment, indicating again that the sample is evenly strained and higher static strain does not necessarily correlate with broader linewidth. **(c)** Histogram of linewidths observed in different sample areas. Both in nano-structured parts (membrane and cantilevers of ∼2 µm thickness) and bulk, broad and narrow linewidths are observed. Narrow and broad linewidth NV centres then form two distinct distributions. **(d)** The same histogram as in (c) resolved by nitrogen isotope. The most striking observation is that no ^{14}NV showed broad linewidths and no ^{15}NV showed narrow linewidths. **(e)** and **(f)** show empirical (i.e. directly obtained from the data set as opposed to theoretically calculated) cumulative distribution functions (ECDFs) of the data, resolved by sample-location (e) and isotope (f) (in (f); solid lines represent data, dotted lines indicate a fit produced by integrating the normal distribution corresponding to the data)). Optical coherence is not affected by sample location: in both nano-structured and bulk areas, the probability of observing a linewidth $\lesssim$2.2 GHz is $\approx$50%. On the other hand, coherence is influenced by whether the nitrogen forming the NV was pre-existing in the diamond or implanted. It is interesting to note that the ECDF for the unlabelled NV centre linewidths is well fitted by a linear combination of two distinct distributions. This indicates that there is no unknown third distribution or correlation in the data.

In Fig. 10(d), the same histogram is depicted, this time resolved by nitrogen isotope. Although there remain unlabelled defects, the narrow-linewidth-distribution strikingly shows no labelled NV centres produced from ion-implantation (i.e. ^{15}N), while the broad-linewidth distribution contains no labelled NV centres produced from naturally occurring nitrogen (i.e. ^{14}N). In Fig. 10(e) and (f), the empirical (i.e. obtained directly from the dataset) cumulative distribution function (ECDF, the integral of the distributions shown in Fig. 10(b) and (e)) of the data is shown, again resolved by sample location (e) and by isotope (f). The value of the ECDF at a certain linewidth indicates the probability to measure a linewidth less or equal to that linewidth. Fig. 10(c) then indicates that in 50% of all cases we observe a linewidth below 2.2 GHz in both sample areas, reinforcing the result that sample location does not affect the optical coherence of the centres down to membrane thickness of ∼2 µm. Fig. Fig. 10(f) clearly indicates prominent differences between the isotopes, i.e. between natural and implanted NV centres. For ^{14}NV centres, 50% of the optical linewidths are ≤0.2 GHz whereas for their counterparts produced from implanted ^{15}N, 50% of the linewidths are ≤15 GHz. Furthermore, the ECDF for the unlabelled centres is a combination of a narrow linewidth distribution and a broad linewidth distribution; the fit for it is produced by a linear combination of two distinct distributions, which indicates that there is no unknown third distribution associated with the linewidths.

We note that for a number of NV centres, the isotopic identification by pODMR remained inconclusive, since a clear hyperfine structure could not be resolved. This could be caused by various reasons, such as poorly chosen Rabi pulse-times, interactions with nearby ^{13}C spins, or simply the appearance of several NV centres within one confocal spot.[48]

In conclusion, our data show that NV centres produced from nitrogen-ion implantation exhibit inferior optical coherence compared to NV centres that originate from naturally occurring nitrogen in the diamond lattice. Adding significant statistical evidence to this phenomenon, this result agrees with a previous study conducted by van Dam et al.[12] Damage induced to the lattice in the implantation process or other unknown processes seem to have a detrimental effect on the optical coherence of these centres. The exact mechanism that causes this effect cannot be deduced from the data of this study and further research needs to be conducted to illuminate the origin of this phenomenon. NV centres produced from nitrogen ion-implantation and subsequent annealing are therefore not suitable for applications that require high optical coherence. NV centres intended for applications that require coherent photons should therefore be created by different techniques. Possible alternatives to nitrogen-ion implantation are carbon-ion implantation,[49] electron irradiation,[50] or laser writing[44] to create vacancies in the diamond lattice. Subsequent annealing will form NV centres only from naturally occurring nitrogen. The process of nitrogen ion-implantation is however still useful to create centres that are used in the context of quantum sensing, since spin coherence, the main benchmark e.g. for NV magnetometry, seems to be unaffected by the detrimental effects of this technique.

3.2 SiV Optical Coherence in Nano-Pillars

The SiV centre combines outstanding photonic properties and an optically addressable spin, which together allow all optical spin manipulation.[21] This makes the SiV centre an interesting alternative to the NV centre as a spin-photon interface in quantum information science, but it also offers very interesting perspective for quantum sensing, specifically in the realm of single-spin microscopy and magnetometry. While the NV centre is suitable for magnetometry at both room temperature[51] (RT) and low temperature[8] (LT), ultra-low temperature magnetometry at temperatures below 1 K has not yet been demonstrated. Microwave control of the NV centre is very challenging in the mK regime due to e.g. excess heating and all-optical control of the NV spin is not generally applicable to all NVs and under arbitrary external fields.[19] The SiV centre is thus a versatile alternative to the NV centre for this specific application, even more so because it can be more easily used in high bias-fields. The combination of mK temperatures and high magnetic fields would allow, for example, to investigate the rich and exotic physics of strongly correlated electron-systems.[52] The elusive features of such systems demand new technologies to efficiently probe them, the development of which is the overarching goal of this project.

Building on our group's experience with scanning-probe configuration magnetometry,[39] we aim at creating all-diamond scanning-probe tips with SiV centres for use in ultra-low temperature, where the SiV exhibits attractive spin properties, comparable to the NV. To this end, we investigate the photonic properties of SiV centres in diamond nano-pillars by measuring optical spectra and second-order correlation functions g^2 at RT (Sect. 3.2.1), and optical spectra and photoluminescence excitation (PLE) at LT (Sect. 3.2.2) with a special focus on the optical coherence of the centres. This investigation provides valuable information for the fabrication of all-diamond scanning-probe tips, specifically on how to create optically coherent single SiV centres in nano-pillars. Narrow-band SiV PL is of paramount importance when optically addressing individual spin states, and thus a prerequisite for controlling and using the SiV for magnetometry. Finally, we estimate the sensitivity of the SiV centre to magnetic fields in Sect. 3.2.3.

3.2.1 High-Temperature Annealing of the Diamond Lattice

Sample #2 contains shallow (∼50 nm from the surface) SiV centres in diamond nano-pillars created by silicon ion-implantation and subsequent annealing of the sample. According to literature, high-temperature annealing of the sample improves the photonic properties of the centres.[15] In this experiment, we investigate the effect of an additional high-temperature annealing step on the photonic properties of the SiV. As outlined in the previous chapter, we perform the same annealing procedure two times, the first time before and the second time after nano-structuring, in the hope of healing some of the damage that is introduced in the implantation and fabrication processes.

To investigate the effect of the second anneal, we measure spectra and second-order correlation functions $g^{(2)}$ of individual pillars in two different pillar fields before and after the second anneal (for saturation curves to analyse the $g^{(2)}$ data, compare appendix D). The $g^{(2)}$ measurement can be used to investigate the quantum nature of an emitter, and for a perfect single-photon emitter, $g^{(2)}(0) = 0$.[53] This means that there is zero probability that two photons are incident on two separate detectors at the same time, which is only possible for a single-photon source. The single emitter regime is considered to be $g^{(2)}(0) < 0.5$, indicating the presence of the $|1\rangle$ Fock state[54] (c.f. also for example Gerry & Knight[55]). A typical result of our study is depicted in

Fig. 11 for one of the investigated SiVs. Indeed, we find that after the second anneal, emission of the centre at the ZPL at 738 nm increases by a factor of ∼30 in this particular pillar. Additionally, we observe that pillars which did not show SiV emission before the second annealing procedure consistently do so after. This points to the formation of additional SiV centres during the second anneal. The phonon sideband is also affected by a rise in counts (see Fig. 11(a) and (b)) on the spectrometer. The second-order correlation function $g^{(2)}$ shows an equally drastic change with annealing. In Fig. 11(c) and (d), the normalised and background-corrected $g^{(2)}$ (c.f. App. D for details on the background correction procedure) is shown along with a fit according to $g^{(2)}(t) = 1 - a \cdot \exp(\frac{-|t-b|}{c})$, following Brouri et al.[56] and Neu et al.[57] Before the second anneal, this particular pillar seemed to host a single centre, indicated by a $g^{(2)}$-dip below 0.5. After the second anneal we find $g^{(2)}(t = 0\,\text{ns}) \sim 0.93$, indicating a large number of emitters in this pillar.

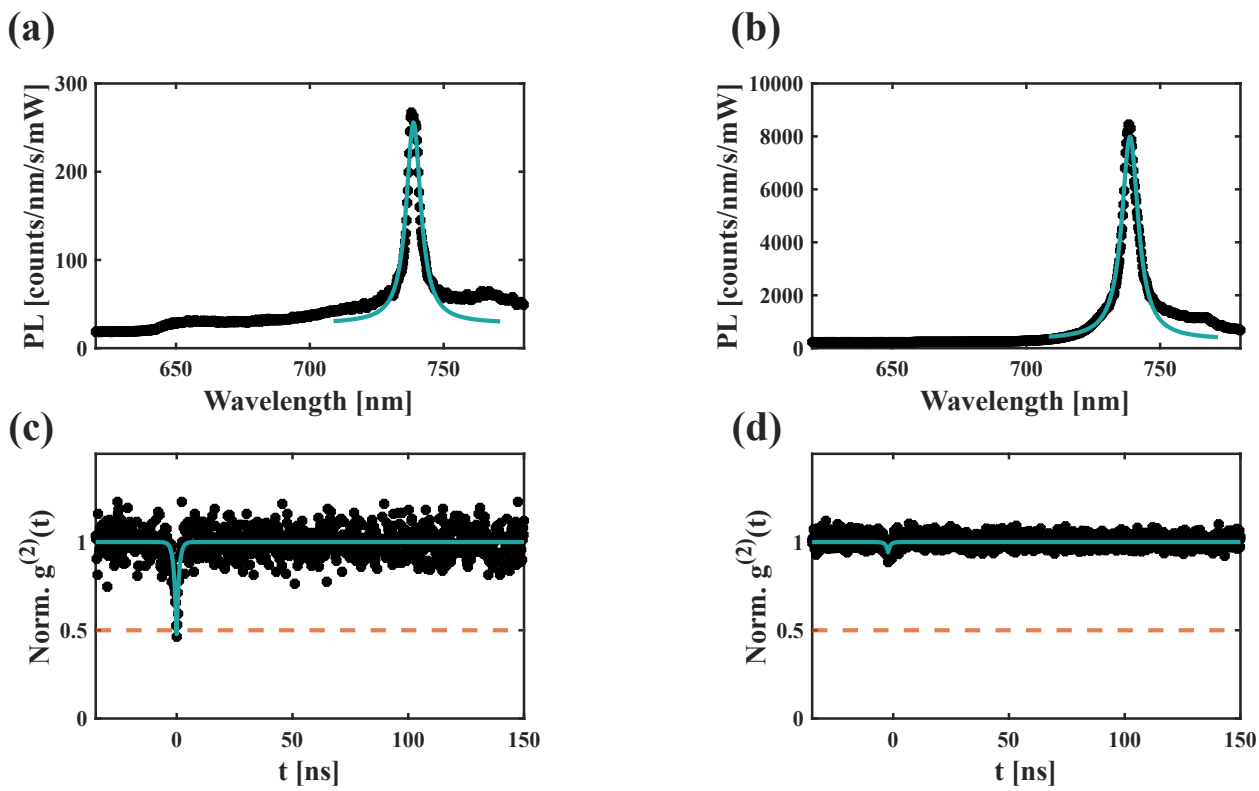

Fig. 11: **(a)** Optical spectrum measured from a single pillar in one of the pillar fields with small mean-diameter (∼ 290 nm) pillars along with a Lorentzian fit, showing the characteristic SiV-ZPL emission around 738 nm. **(b)** Normalised spectrum of the same pillar after the second anneal, showing a ∼30-fold increase in emission at the ZPL compared to (a). **(c)** Second order correlation function $g^{(2)}(t)$ of the pillar before the second anneal (fit in mint). The orange dotted line indicates the cross-over to the single-emitter regime. **(d)** $g^{(2)}(t)$ after the second anneal, indicating a significant increase in the number of emitters per pillar.

This result has implications for fabrication of further samples, indicating the need for careful tuning of the geometrical parameters of the pillars and of ion-implantation density. Our data indicate that the second annealing procedure after nano-structuring increases the number of emitters in a single pillar, which leads to increased emission counts. We cannot deduce if the repairing of damage (induced by ion-implantation and nano-structuring) to the diamond lattice that accompanies high temperature annealing[41] leads to a higher quality of emission since the increased number of emitters obscures this effect. This is in contrast to results of

Evans et al., who do not observe an increased yield after the second anneal.[15] It is important to note, however, that we anneal at higher temperature (1300 °C instead of 1100 °C used by Evans et al.[15]), after nano-structuring the sample, and we already employ a high-temperature step in the first annealing procedure. These differences complicate a direct comparison between the two works and further investigations are required to clarify the role of sample annealing in SiV formation.

We will now move on to the low-temperature results of our study and investigate the optical coherence of our shallow SiV centres in diamond nano-pillars.

3.2.2 Optical Coherence

We investigated the optical coherence of the SiV centre in a nano-structured photonic-device by cooling down our sample to around 4 K. As outlined before, NV centres usually show deterioration in optical coherence as a result of nano-structuring, (Sect. 3.1), resulting in suboptimal photon-indistinguishability for NV centres formed by nitrogen implantation. It would therefore be interesting to establish whether the superior optical qualities of the SiV centre persist also in nano-structures.

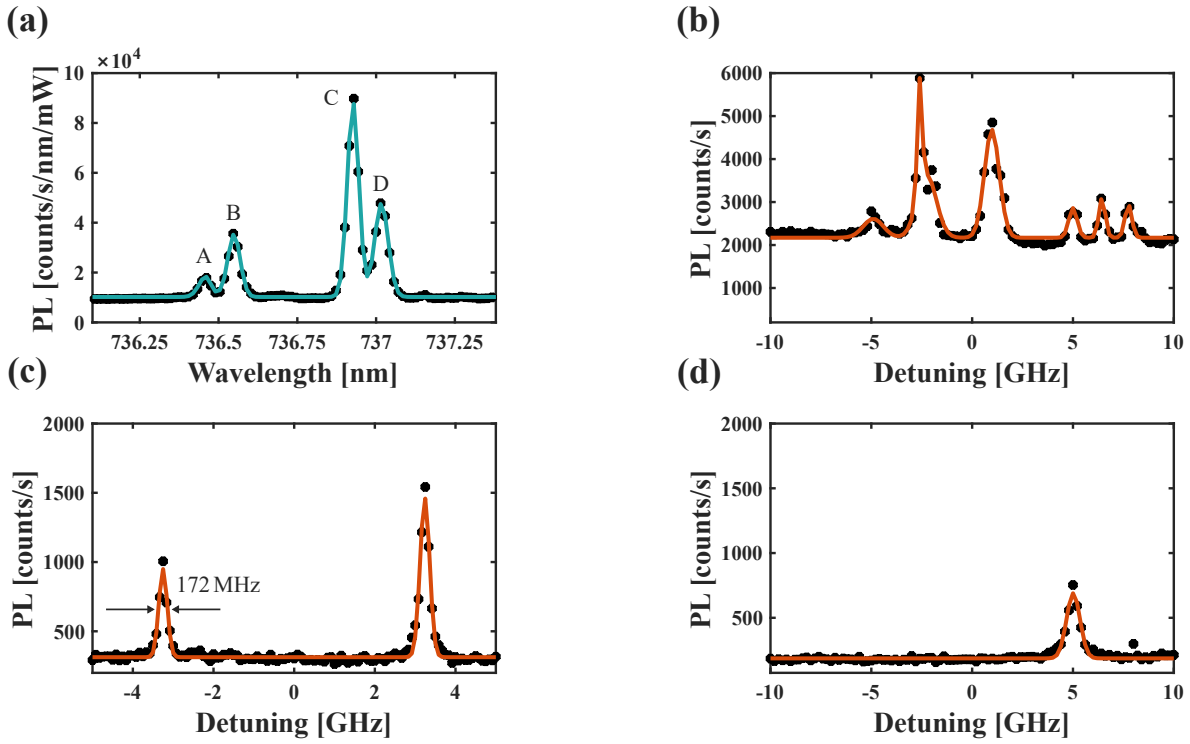

Fig. 12: **(a)** Low-temperature optical spectrum of one of the pillars, revealing the characteristic four-line fine-structure of the SiV centre (data in black dots and Gaussian fit in mint). **(b)** PLE measurement of transition C on one of the pillars (data in black dots, Gaussian fit in orange). This measurement confirms findings from room temperature $g^{(2)}$ measurements, since many PLE peaks visible indicate that we probe several SiV centres simultaneously. The range of Gaussian FWHM linewidths in these six peaks is 195 MHz to 824 MHz. It is also interesting to note the high background counts in these data, probably originating from the high number of emitters in this pillar. **(c)** Transition C of another pillar showing only two peaks, with FWHM linewidths of 172 MHz and 197 MHz respectively, thus showing coherent emission from SiV centres in nano-pillars. **(d)** Resonant excitation spectrum of transition B from the same pillar as in (c), exhibiting a single line with FWHM of 550 MHz.

A typical low-temperature optical spectrum of a single SiV centre in a nanopillar is depicted in Fig. 12(a) (data in black dots and Gaussian fit in mint). All four zero-field transitions {A,B,C,D} of the SiV are clearly discernible. We can, among other quantities, deduce the temperature of the diamond lattice by fitting the theoretical model introduced in Sect. 1.2.2 to the experimental data obtained in an optical spectrum. The distribution of the relative intensities suggests a sample temperature of 8.5 K (cf. Sect. 1.2.2 and App. C for details on the temperature dependence of the relative intensities).

Fig. 12(b)–(d) show PLE data (recorded the same way as for the NV centres in the previous section) for two SiV centres (data in black, Gaussian fits in orange). Data were acquired with different powers for the red resonant laser and the green repump laser (with the same pulse sequence as for the NV centre in Sect. 3.1) to reduce power broadening. The data depicted here were recorded with 30-70 nW of red laser and 1-14 µW of green laser. Fig. 12(b) (30 nW red, 1 µW green) shows six PLE peaks with a range of Gaussian FWHM linewidths 195-824 MHz. These data show that we are probing transitions of several separate SiV centres emitting in a narrow spectral window, indicating low static strain. Fig. 12(c) (30 nW red, 14 µW green) shows transition C of a different pillar with only two peaks, suggesting that fewer defects are present in this pillar. The FWHM linewidths of those two lines are 197 MHz and 172 MHz respectively, showing coherent photon emission of shallow SiV centres in nano-pillars, achieving near lifetime limited (∼100 MHz) values. Finally, Fig. 12(d) (70 nW red, 5 µW green) shows the linewidth of transition B of the same pillar as in (c), with a single line with a FWHM linewidth of 550 MHz showing that we are able to address the transitions individually and that we can select the one most suited to our needs in magnetometry (see Sect. 1.2.2). In this case, the significant difference in linewidths between Fig. 12(c) and (d) most likely originates from the different powers of the red excitation laser used for the two measurements, although power broadening arising from the different polarisations associated with the transitions[30] is another possible explanation. The difference between the Gaussian fit and the data depicted in Fig. 12(d) points in any case to power broadening of the line. We mostly probed transition C because it is the strongest of the zero-field transitions, but in principle, all four transitions can be addressed in the same way. The narrowest linewidth obtained in this study is 172 MHz, close to the lifetime limit.

To place these results in context, it is instructive to compare them to recent developments in the field. Studies reporting SiV linewidths of ≤0.5 GHz either do so with bulk-like SiV centres (0.1-6.5 µm from the surface),[18,58,59] or with SiV centres embedded in nano-diamonds,[53,60,61] where deterministic placement of the defect is not possible. Additionally, there are some efforts to place the SiV in nano-structures such as diamond nano-cavities[62], nano-beam waveguides[15] or cantilevers[63] and investigate its optical coherence there. Indeed, SRIM (Stopping and Range of Ions in Matter) simulations place the depth of our SiV centres in the pillars at around 50 nm, making them some of the shallowest SiV centres with close to lifetime-limited optical coherence measured to date.

3.2.3 SiV Sensitivity to DC-Magnetic Fields

Given our ultimate goal of using SiV centres as nanoscale magnetometers, we will now estimate their sensitivity to dc-magnetic fields.

The sensitivity is defined as the minimal dc-magnetic field change detectable for a signal-to-noise ratio of one[64] (assuming Poissonian photon shot-noise):

$$\mathrm{SNR} = 1 = \frac{\text{Change in fluorescence}}{\text{Photon shot-noise}} = \frac{\frac{\partial I}{\partial B_{\min}} \cdot \delta B_{\min} \cdot \Delta t}{\sqrt{I \cdot \Delta t}}, \tag{3.1}$$

with I the count rate at the measurement point, $\delta B_{\min}$ the minimal detectable magnetic field change and Δt the measurement duration. Thus defining the sensitivity, η, as[26]

$$\eta = \delta B_{\min} \sqrt{\Delta t} = \frac{\sqrt{I}}{\partial I / \partial B}. \tag{3.2}$$

In the spirit of the PLE measurements with the SiV centre in the previous section, and following the example of the NV,[26] the easiest scheme to measure a dc-magnetic field, then, would be to evaluate the change of the PLE spectrum as a magnetic field is applied. For this, one would fix the resonant laser to the maximal slope of a given PLE peak and monitor the change in fluorescence as the magnetic field changes. It is now straight forward to calculate

$$\frac{\partial I}{\partial B} = \frac{\partial I}{\partial \omega} \frac{\partial \omega}{\partial B}. \tag{3.3}$$

Assuming a Gaussian peak for the PLE measurement, we find the maximum of $\frac{\partial I}{\partial \omega}$ as

$$\frac{\partial I}{\partial \omega}_{\max} = \frac{2\sqrt{\ln 2}}{e^{1/2}} \frac{C \cdot I_{\max}}{\gamma}, \tag{3.4}$$

where $I_{\max}$ is the maximum count rate and γ the FWHM linewidth of the SiV. We have additionally introduced a contrast factor, $C = 1 - I_{\min}/I_{\max}$, where $I_{\min}$ are the background counts. The term $\frac{\partial \omega}{\partial B}$ can either be measured experimentally by recording magnetic field dependant PLE spectra (cf. for example Pingault et al.)[65] or by calculating $\frac{\partial \omega}{\partial B}$ theoretically from the Hamiltonian (c.f. Fig. 6(c)). By inserting Eq. 3.4 and Eq. 3.3 into Eq. 3.2, we obtain

$$\eta_{\mathrm{PLE}} = \frac{1}{\sqrt{4 \ln 2 e^{-1/2}}} \frac{\gamma}{\sqrt{C \cdot I_{\max}}} \left(\frac{\partial \omega}{\partial B} \right)^{-1}. \tag{3.5}$$

Assuming the narrowest FWHM linewidth of our SiV centres of $\gamma_{\mathrm{PLE}} = 172\,\mathrm{MHz}$, a count-rate of $I_{\max} = 1000\,\mathrm{counts/s}$, a typical PLE contrast of $C = 0.8$, and $\frac{\partial \omega}{\partial B} = 28\,\mathrm{GHz/T}$ from the model in Sect. 1.2.2, we obtain a sensitivity of $\eta_{\mathrm{PLE}} = 167\,\mu\mathrm{T}/\sqrt{\mathrm{Hz}}$.

In an optical spin-resonance (SR) experiment, we can perform the same calculation. Let us first propose the measurement. We apply an off-axis bias magnetic field to the SiV that splits its spin-states. Now we initialise the SiV spin for example in the $|m_S = {}^1/_2\rangle$ state of one of the ground states of the SiV. In the next step, we use a resonant red laser and its sideband, generated by an electro-optical modulator (EOM), to resonantly excite transitions between the two ground state spin levels $|m_S = \pm{}^1/_2\rangle$ and a common excited state, thereby forming a Λ-system and transferring the spin-population to $|m_S = -{}^1/_2\rangle$ in the ground state with an optical π-pulse.[21] If we sweep the EOM modulation frequency and monitor the phonon sideband (PSB) emission, we will thus sweep across the spin-resonance of the SiV, in the spirit of an ODMR measurement for an NV centre. This procedure results in a peak in the spectrum, whose width is determined by the coherence time of the SiV, T_2^*. Thus the linewidth is $\gamma_{SR} = 0.44/T_2^*$, given by the time-bandwidth product for a Gaussian peak.

By inserting a count rate of $I_{max} = 1000\,\text{counts/s}$, $\frac{\partial\omega}{\partial B} = 28\,\text{GHz/T}$, $\gamma_{SR} = 0.44/T_2^*$ for $T_2^* = 1.5\,\mu\text{s}$,[18] and a typical PLE contrast of $C = 0.8$ into Eq. (3.5), we obtain a sensitivity of $\eta_{SR} = 286\,\text{nT}/\sqrt{\text{Hz}}$, improving the sensitivity by three orders of magnitude. Increasing the spin-coherence time by dynamical decoupling schemes will further enhance the sensitivity of the SiV.

The fundamental limit of the sensitivity is given by[64]

$$\eta_{min} \approx \frac{\sqrt{2e}}{\gamma_e K \sqrt{T_2^*}}, \tag{3.6}$$

where γ_e the electron gyromagnetic ratio, $K \leq 1$ a dimensionless constant describing readout efficiency, and T_2^* the coherence-time of the spin. By choosing $K = 1$ since single shot spin readout has successfully been demonstrated for the SiV centre,[18] and again $T_2^* = 1.5\,\mu\text{s}$, we obtain $\eta_{min} = 68\,\text{nT}/\sqrt{\text{Hz}}$ as the fundamental limit of the SiV dc-magnetic field sensitivity.

The results of this section, as well as the considerations of SiV sensitivity to dc-magnetic fields, establish the SiV centre as a promising quantum sensor with applications in all-optical ultra-low temperature high-field magnetometry.

Chapter 4

Summary and Outlook

In this thesis, we performed in-depth studies of the optical properties of two colour defects in diamond, the NV centre and the SiV centre, with special emphasis on optical coherence.

- We investigated the impact of nitrogen ion-implantation on optical coherence of single NV centres by characterising 51 NV centres in a post-fabrication ^{15}N-implanted sample and we labelled the emitters according to their nitrogen isotope, thereby establishing a dataset that allows statistical analysis of the NV creation process. We find that a change in sample area did not affect optical coherence of single NV centres, both bulk and nano-structured parts of the sample contain broad and narrow linewidth NV centres. However, we discover that no NV centre formed from implanted nitrogen exhibits narrow emission below 1 GHz, and no centre formed from natural nitrogen dopants in the diamond matrix shows broad emission above 1 GHz. We also established that static strain does not explain this discrepancy between implanted NV centres and natural NV centres.

- For the SiV centre, we have carried out theoretical calculations of their optical spectra. These allow us to fit our experimental data and thereby describing the physics of the defect by considering the relevant electronic interactions. Further, we carried out optical characterisation of shallow (50 nm from the diamond surface) SiV centres in diamond nano-pillars at both room temperature and 4 K. These studies shed light onto the role of a second high-temperature anneal for optical emission quality of the SiV centres. At low temperature, we observe strong and coherent emission (consistent linewidths below 1 GHz) in each characterised nano-pillar, and we are able to resolve and drive the individual transitions of the defect. Additionally, we estimate the dc-magnetic field sensitivity of the SiV centre, establishing a sensitivity for optical lifetime experiments of $\eta_{\mathrm{PLE}} = 167\,\mu\mathrm{T}/\sqrt{\mathrm{Hz}}$ and for spin-resonance experiments of $\eta_{\mathrm{SR}} = 286\,\mathrm{nT}/\sqrt{\mathrm{Hz}}$.

Both experiments conducted in this thesis have implications for the future use and fabrication of NV and SiV centres: our results for the NV centre show that it is nitrogen ion-implantation itself that produces NV centres with low optical coherence, agreeing with a previous study by van Dam et al.[12] and adding significant statistical evidence to this phenomenon. It is not necessarily, as previously thought,[10] the combination of ion-implantation and nano-structuring that results in poor optical coherence. Significant damage to the diamond lattice produced by implanted nitrogen ions leads to inferior optical coherence properties of the resulting NV centres. Naturally occurring nitrogen that combines with vacancies to form NV centres circumvents this limitation, however, one still needs to create such vacancies in the lattice. While the implanted nitrogen ions do not produce high-quality

NV centres, the process of ion-implantation creates vacancies in the diamond host, and these vacancies combine with naturally occurring nitrogen. NV centres formed in this way do not suffer from the poor optical coherence of their implanted counterparts, making alternative approaches to vacancy creation such as laser writing[44] all the more promising. Steps are already under way to systematically characterise NV centres created in this manner and to incorporate the resulting narrow-linewidth NVs into optical cavities. Additionally, vacancy creation by carbon ion-implantation[49] or electron irradiation[50] with subsequent annealing offer additional alternative approaches to NV centre creation. Thus is seems that the NV centre is still a promising candidate for scalable qubit systems, if alternatives to nitrogen ion-implantation will not result in other, still unknown effects that limit optical coherence.

Our results for the SiV centre in nano-pillars pave the way for ultra-low temperature, high-field scanning probe magnetometry. We show that SiV centres created by ion-implantation and annealing retain excellent optical coherence in our nano-structures, and we can address narrow individual transitions of the defect resonantly, an important milestone towards all-optical control of the SiV's electronic spin. For future applications of the SiV centre, we will now need to carefully investigate the parameters for creating nano-pillars and SiVs, such as implantation density, number of anneals, annealing temperature,[15] and geometry of the pillars. To this end, additional measurements on a different sample than the one used in this investigation were conducted in our research group. The resolution in magnetometry is directly affected by the distance of the sensor (i.e. the SiV) to the sample under investigation.[26] It is therefore a very important task to be able to create optically coherent SiV centres as close to the diamond surface as possible. This is why the sample for the additional measurements was implanted with ^{28}Si ions at lower energy (25 keV instead of 80 keV) and with the same density of 1.5×10^{11} ions/cm^2. The SiV centres created by annealing will therefore be found at a depth of ∼20 nm from the diamond surface according to SRIM calculations, 30 nm closer to the surface than the SiVs in this thesis (depth ∼50 nm). Photoluminescence excitation (PLE) measurements in this sample before and after the second annealing procedure revealed FWHM linewidths of 10-20 GHz. These broad linewidths may be attributed to the shallow depths of these defect centres. However, for NV centres, there is experimental evidence of optically coherent emission very close (∼10 nm) to the surface of the diamond.[41] The superior optical properties of the SiV centre suggest that coherent optical emission close to the diamond surface should be possible as well, but further systematic studies are required to verify this. From present data, we can only establish coherent optical emission from SiVs by implanting Si ions at 80 keV. As for implantation density, the additional sample confirms that nano-pillars with single SiV centres can be found after the first annealing procedure with a Si → SiV conversion efficiency of ∼0.03. A second high-temperature annealing procedure produces once more a higher SiV yield, increasing the conversion efficiency to ∼0.18. Pillars with single SiVs could not be found, indicating the need for implantation densities lower than 1.5×10^{11} ions/cm^2. Although we have not extensively studied the conversion efficiency, we estimate from this data that an implantation density of $\sim 1 \times 10^{10}$ ions/cm^2 in combination with two high-temperature annealing procedures will yield single SiVs in nano-pillars with mean diameter of ∼290 nm.

Additionally, we will continue to investigate and master the coherent control of the defect, for example by performing coherent population trapping[65] (CPT) on the defects in our pillars. Lastly, we will implement SiV-based nanoscale magnetometry at mK-temperatures by fabricating all-diamond scanning probes with incorporated, coherent SiV spins.

Bibliography

[1] I. Aharonovich, S. Castelletto, D. A. Simpson, C.-H. Su, A. D. Greentree, and S. Prawer, *Diamond-based single-photon emitters*, Reports on Progress in Physics **74**, 076501 (2011).

[2] J. M. Smith, S. A. Meynell, J. A. C. Bleszynski, and J. Meijer, *Colour centre generation in diamond for quantum technologies*, Nanophotonics **8**, 1889 (2019).

[3] M. W. Doherty, N. B. Manson, P. Delaney, F. Jelezko, J. Wrachtrup, and L. C. L. Hollenberg, *The nitrogen-vacancy colour centre in diamond*, Physics Reports **528**, 1 (2013).

[4] H. Bernien, B. Hensen, W. Pfaff, G. Koolstra, M. S. Blok, L. Robledo, T. H. Taminiau, M. Markham, D. J. Twitchen, L. Childress, and R. Hanson, *Heralded entanglement between solid-state qubits separated by three metres*, Nature **497**, 86 (2013).

[5] W. Pfaff, B. J. Hensen, H. Bernien, S. B. v. Dam, M. S. Blok, T. H. Taminiau, M. J. Tiggelman, R. N. Schouten, M. Markham, D. J. Twitchen, and R. Hanson, *Unconditional quantum teleportation between distant solid-state quantum bits*, Science **345**, 532 (2014).

[6] B. Hensen, H. Bernien, A. E. Dréau, A. Reiserer, N. Kalb, M. S. Blok, J. Ruitenberg, R. F. L. Vermeulen, R. N. Schouten, C. Abellán, W. Amaya, V. Pruneri, M. W. Mitchell, M. Markham, D. J. Twitchen, D. Elkouss, S. Wehner, T. H. Taminiau, and R. Hanson, *Loophole-free Bell inequality violation using electron spins separated by 1.3 kilometres*, Nature **526**, 682 (2015).

[7] P. Maletinsky, S. Hong, M. S. Grinolds, B. Hausmann, M. D. Lukin, R. L. Walsworth, M. Loncar, and A. Yacoby, *A robust scanning diamond sensor for nanoscale imaging with single nitrogen-vacancy centres*, Nature Nanotechnology **7**, 320 (2012).

[8] L. Thiel, Z. Wang, M. A. Tschudin, D. Rohner, I. Gutiérrez-Lezama, N. Ubrig, M. Gibertini, E. Giannini, A. F. Morpurgo, and P. Maletinsky, *Probing magnetism in 2D materials at the nanoscale with single-spin microscopy*, Science **364**, 973 (2019).

[9] M. Fukami, C. Yale, P. Andrich, X. Liu, F. Heremans, P. Nealey, and D. Awschalom, *All-Optical Cryogenic Thermometry Based on Nitrogen-Vacancy Centers in Nanodiamonds*, Physical Review Applied **12**, 014042 (2019).

[10] D. Riedel, I. Söllner, B. J. Shields, S. Starosielec, P. Appel, E. Neu, P. Maletinsky, and R. J. Warburton, *Deterministic Enhancement of Coherent Photon Generation from a Nitrogen-Vacancy Center in Ultrapure Diamond*, Physical Review X **7**, 031040 (2017).

[11] J. O. Orwa, C. Santori, K. M. C. Fu, B. Gibson, D. Simpson, I. Aharonovich, A. Stacey, A. Cimmino, P. Balog, M. Markham, D. Twitchen, A. D. Greentree, R. G. Beausoleil, and S. Prawer, *Engineering of nitrogen-vacancy color centers in high purity diamond by ion implantation and annealing*, Journal of Applied Physics **109**, 083530 (2011).

[12] S. B. van Dam, M. Walsh, M. J. Degen, E. Bersin, S. L. Mouradian, A. Galiullin, M. Ruf, M. IJspeert, T. H. Taminiau, R. Hanson, and D. R. Englund, *Optical coherence of diamond nitrogen-vacancy centers formed by ion implantation and annealing*, Physical Review B **99**, 161203 (2019).

[13] E. Neu, D. Steinmetz, J. Riedrich-Möller, S. Gsell, M. Fischer, M. Schreck, and C. Becher, *Single photon emission from silicon-vacancy colour centres in chemical vapour deposition nano-diamonds on iridium*, New Journal of Physics **13**, 025012 (2011).

[14] S. Lagomarsino, A. M. Flatae, S. Sciortino, F. Gorelli, M. Santoro, F. Tantussi, F. De Angelis, N. Gelli, F. Taccetti, L. Giuntini, and M. Agio, *Optical properties of silicon-vacancy color centers in diamond created by ion implantation and post-annealing*, Diamond and Related Materials **84**, 196 (2018).

[15] R. E. Evans, A. Sipahigil, D. D. Sukachev, A. S. Zibrov, and M. D. Lukin, *Narrow-Linewidth Homogeneous Optical Emitters in Diamond Nanostructures via Silicon Ion Implantation*, Physical Review Applied **5**, 044010 (2016).

[16] K. D. Jahnke, A. Sipahigil, J. M. Binder, M. W. Doherty, M. Metsch, L. J. Rogers, N. B. Manson, M. D. Lukin, and F. Jelezko, *Electron–phonon processes of the silicon-vacancy centre in diamond*, New Journal of Physics **17**, 043011 (2015).

[17] J. N. Becker and C. Becher, *Coherence Properties and Quantum Control of Silicon Vacancy Color Centers in Diamond*, physica status solidi (a) **214**, 1700586 (2017).

[18] D. Sukachev, A. Sipahigil, C. Nguyen, M. Bhaskar, R. Evans, F. Jelezko, and M. Lukin, *Silicon-Vacancy Spin Qubit in Diamond: A Quantum Memory Exceeding 10 ms with Single-Shot State Readout*, Physical Review Letters **119**, 223602 (2017).

[19] A. Wickenbrock, H. Zheng, L. Bougas, N. Leefer, S. Afach, A. Jarmola, V. M. Acosta, and D. Budker, *Microwave-free magnetometry with nitrogen-vacancy centers in diamond*, Applied Physics Letters **109**, 053505 (2016).

[20] C. G. Yale, B. B. Buckley, D. J. Christle, G. Burkard, F. J. Heremans, L. C. Bassett, and D. D. Awschalom, *All-optical control of a solid-state spin using coherent dark states*, Proceedings of the National Academy of Sciences **110**, 7595 (2013).

[21] J. N. Becker, B. Pingault, D. Groß, M. Gündoğan, N. Kukharchyk, M. Markham, A. Edmonds, M. Atatüre, P. Bushev, and C. Becher, *All-Optical Control of the Silicon-Vacancy Spin in Diamond at Millikelvin Temperatures*, Physical Review Letters **120**, 053603 (2018).

[22] C. J. Meara, M. J. Rayson, P. R. Briddon, and J. P. Goss, *Density functional theory study on magnetically detecting positively charged nitrogen-vacancy center in diamond*, Physical Review B **100**, 104108 (2019).

[23] M. S. Barson, E. Krausz, N. B. Manson, and M. W. Doherty, *The fine structure of the neutral nitrogen-vacancy center in diamond*, Nanophotonics **8**, 1985 (2019).

[24] R. Schirhagl, K. Chang, M. Loretz, and C. L. Degen, *Nitrogen-Vacancy Centers in Diamond: Nanoscale Sensors for Physics and Biology*, Annual Review of Physical Chemistry **65**, 83 (2014).

[25] S. Hong, M. S. Grinolds, L. M. Pham, D. L. Sage, L. Luan, R. L. Walsworth, and A. Yacoby, *Nanoscale magnetometry with NV centers in diamond*, MRS Bulletin **38**, 155 (2013).

[26] L. Rondin, J.-P. Tetienne, T. Hingant, J.-F. Roch, P. Maletinsky, and V. Jacques, *Magnetometry with nitrogen-vacancy defects in diamond*, Reports on Progress in Physics **77**, 056503 (2014).

[27] L. Childress and R. Hanson, *Diamond NV centers for quantum computing and quantum networks*, MRS Bulletin **38**, 134 (2013).

[28] B. Smeltzer, L. Childress, and A. Gali, *13C hyperfine interactions in the nitrogen-vacancy centre in diamond*, New Journal of Physics **13**, 025021 (2011).

[29] B. Green, S. Mottishaw, B. Breeze, A. Edmonds, U. D'Haenens-Johansson, M. Doherty, S. Williams, D. Twitchen, and M. Newton, *Neutral Silicon-Vacancy Center in Diamond: Spin Polarization and Lifetimes*, Physical Review Letters **119**, 096402 (2017).

[30] C. Hepp, T. Müller, V. Waselowski, J. N. Becker, B. Pingault, H. Sternschulte, D. Steinmüller-Nethl, A. Gali, J. R. Maze, M. Atatüre, and C. Becher, *Electronic Structure of the Silicon Vacancy Color Center in Diamond*, Physical Review Letters **112** (2014).

[31] A. Sipahigil, K. Jahnke, L. Rogers, T. Teraji, J. Isoya, A. Zibrov, F. Jelezko, and M. Lukin, *Indistinguishable Photons from Separated Silicon-Vacancy Centers in Diamond*, Physical Review Letters **113**, 113602 (2014).

[32] B. C. Rose, D. Huang, Z.-H. Zhang, P. Stevenson, A. M. Tyryshkin, S. Sangtawesin, S. Srinivasan, L. Loudin, M. L. Markham, A. M. Edmonds, D. J. Twitchen, S. A. Lyon, and N. P. d. Leon, *Observation of an environmentally insensitive solid-state spin defect in diamond*, Science **361**, 60 (2018).

[33] A. Gali and J. R. Maze, *Ab initio study of the split silicon-vacancy defect in diamond: Electronic structure and related properties*, Physical Review B **88**, 235205 (2013).

[34] C. Hepp, *Electronic structure of the silicon vacancy color center in diamond*, Thesis, Universität des Saarlandes (2014).

[35] J. N. Becker, *Silicon vacancy colour centres in diamond: coherence properties & quantum control*, Thesis, Universität des Saarlandes (2017).

[36] H. A. Jahn, E. Teller, and F. G. Donnan, *Stability of polyatomic molecules in degenerate electronic states*, Proceedings of the Royal Society of London. Series A - Mathematical and Physical Sciences **161**, 220 (1937).

[37] F. S. Ham, *Dynamical Jahn-Teller Effect in Paramagnetic Resonance Spectra: Orbital Reduction Factors and Partial Quenching of Spin-Orbit Interaction*, Physical Review **138**, A1727 (1965).

[38] C. D. Clark, H. Kanda, I. Kiflawi, and G. Sittas, *Silicon defects in diamond*, Physical Review B **51**, 16681 (1995).

[39] P. Appel, E. Neu, M. Ganzhorn, A. Barfuss, M. Batzer, M. Gratz, A. Tschöpe, and P. Maletinsky, *Fabrication of all diamond scanning probes for nanoscale magnetometry*, Review of Scientific Instruments **87**, 063703 (2016).

[40] A. Barfuss, *Hybrid spin-nanomechanics with single spins in diamond mechanical oscillators*, Thesis, University of Basel (2017).

[41] Y. Chu, N. de Leon, B. Shields, B. Hausmann, R. Evans, E. Togan, M. J. Burek, M. Markham, A. Stacey, A. Zibrov, A. Yacoby, D. Twitchen, M. Loncar, H. Park, P. Maletinsky, and M. Lukin, *Coherent Optical Transitions in Implanted Nitrogen Vacancy Centers*, Nano Letters **14**, 1982 (2014).

[42] N. Bar-Gill, L. M. Pham, A. Jarmola, D. Budker, and R. L. Walsworth, *Solid-state electronic spin coherence time approaching one second*, Nature Communications **4**, 1 (2013).

[43] D. Riedel, *Engineering of the photonic environment of single nitrogen-vacancy centers in diamond*, Thesis, University of Basel (2017).

[44] Y.-C. Chen, B. Griffiths, L. Weng, S. S. Nicley, S. N. Ishmael, Y. Lekhai, S. Johnson, C. J. Stephen, B. L. Green, G. W. Morley, M. E. Newton, M. J. Booth, P. S. Salter, and J. M. Smith, *Laser writing of individual nitrogen-vacancy defects in diamond with near-unity yield*, Optica **6**, 662 (2019).

[45] S. Felton, A. M. Edmonds, M. E. Newton, P. M. Martineau, D. Fisher, D. J. Twitchen, and J. M. Baker, *Hyperfine interaction in the ground state of the negatively charged nitrogen vacancy center in diamond*, Physical Review B **79**, 075203 (2009).

[46] A. Dréau, M. Lesik, L. Rondin, P. Spinicelli, O. Arcizet, J.-F. Roch, and V. Jacques, *Avoiding power broadening in optically detected magnetic resonance of single NV defects for enhanced dc magnetic field sensitivity*, Physical Review B **84**, 195204 (2011).

[47] G. Davies, M. F. Hamer, and W. C. Price, *Optical studies of the 1.945 eV vibronic band in diamond*, Proceedings of the Royal Society of London. A. Mathematical and Physical Sciences **348**, 285 (1976).

[48] L. Schlipf, *Nanoscale electron spin resonance*, Ph.D. thesis, Universität Stuttgart (2017).

[49] K. Ohno, F. Joseph Heremans, C. F. de las Casas, B. A. Myers, B. J. Alemán, A. C. Bleszynski Jayich, and D. D. Awschalom, *Three-dimensional localization of spins in diamond using 12C implantation*, Applied Physics Letters **105**, 052406 (2014).

[50] C. A. McLellan, B. A. Myers, S. Kraemer, K. Ohno, D. D. Awschalom, and A. C. Bleszynski Jayich, *Patterned Formation of Highly Coherent Nitrogen-Vacancy Centers Using a Focused Electron Irradiation Technique*, Nano Letters **16**, 2450 (2016).

[51] K. Jensen, N. Leefer, A. Jarmola, Y. Dumeige, V. Acosta, P. Kehayias, B. Patton, and D. Budker, *Cavity-Enhanced Room-Temperature Magnetometry Using Absorption by Nitrogen-Vacancy Centers in Diamond*, Physical Review Letters **112**, 160802 (2014).

[52] J. L. Gavilano, B. Ambrosini, P. Vonlanthen, J. Hunziker, and H. R. Ott, *Low-temperature NMR studies of strongly correlated electron systems*, Physica B: Condensed Matter **230-232**, 563 (1997).

[53] Y. Zhou, A. Rasmita, K. Li, Q. Xiong, I. Aharonovich, and W.-b. Gao, *Coherent control of a strongly driven silicon vacancy optical transition in diamond*, Nature Communications **8**, 1 (2017).

[54] S. Buckley, K. Rivoire, and J. Vučković, *Engineered quantum dot single-photon sources*, Reports on Progress in Physics **75**, 126503 (2012).

[55] P. K. C. Gerry, *Introductory Quantum Optics* (Cambridge University Press, Cambridge, UK) (2004).

[56] R. Brouri, A. Beveratos, J.-P. Poizat, and P. Grangier, *Photon antibunching in the fluorescence of individual color centers in diamond*, Optics Letters **25**, 1294 (2000).

[57] E. Neu, M. Agio, and C. Becher, *Photophysics of single silicon vacancy centers in diamond: implications for single photon emission*, Optics Express **20**, 19956 (2012).

[58] L. J. Rogers, K. D. Jahnke, T. Teraji, L. Marseglia, C. Müller, B. Naydenov, H. Schauffert, C. Kranz, J. Isoya, L. P. McGuinness, and F. Jelezko, *Multiple intrinsically identical single-photon emitters in the solid state*, Nature Communications **5**, 1 (2014).

[59] T. Schröder, M. E. Trusheim, M. Walsh, L. Li, J. Zheng, M. Schukraft, A. Sipahigil, R. E. Evans, D. D. Sukachev, C. T. Nguyen, J. L. Pacheco, R. M. Camacho, E. S. Bielejec, M. D. Lukin, and D. Englund, *Scalable focused ion beam creation of nearly lifetime-limited single quantum emitters in diamond nanostructures*, Nature Communications **8**, 1 (2017).

[60] U. Jantzen, A. B. Kurz, D. S. Rudnicki, C. Schäfermeier, K. D. Jahnke, U. L. Andersen, V. A. Davydov, V. N. Agafonov, A. Kubanek, L. J. Rogers, and F. Jelezko, *Nanodiamonds carrying silicon-vacancy quantum emitters with almost lifetime-limited linewidths*, New Journal of Physics **18**, 073036 (2016).

[61] K. Li, Y. Zhou, A. Rasmita, I. Aharonovich, and W. Gao, *Nonblinking Emitters with Nearly Lifetime-Limited Linewidths in CVD Nanodiamonds*, Physical Review Applied **6**, 024010 (2016).

[62] R. E. Evans, M. K. Bhaskar, D. D. Sukachev, C. T. Nguyen, A. Sipahigil, M. J. Burek, B. Machielse, G. H. Zhang, A. S. Zibrov, E. Bielejec, H. Park, M. Lončar, and M. D. Lukin, *Photon-mediated interactions between quantum emitters in a diamond nanocavity*, Science **362**, 662 (2018).

[63] Y.-I. Sohn, S. Meesala, B. Pingault, H. A. Atikian, J. Holzgrafe, M. Gündoğan, C. Stavrakas, M. J. Stanley, A. Sipahigil, J. Choi, M. Zhang, J. L. Pacheco, J. Abraham, E. Bielejec, M. D. Lukin, M. Atatüre, and M. Lončar, *Controlling the coherence of a diamond spin qubit through its strain environment*, Nature Communications **9**, 1 (2018).

[64] C. Degen, F. Reinhard, and P. Cappellaro, *Quantum sensing*, Reviews of Modern Physics **89**, 035002 (2017).

[65] B. Pingault, J. N. Becker, C. H. Schulte, C. Arend, C. Hepp, T. Godde, A. I. Tartakovskii, M. Markham, C. Becher, and M. Atatüre, *All-Optical Formation of Coherent Dark States of Silicon-Vacancy Spins in Diamond*, Physical Review Letters **113**, 263601 (2014).

[66] A. N. L. Mariot, *Group Theory and Solid State Physics* (Prentice-Hall, Inc., Englewood Cliffs, N. J.) (1962).

[67] M. Tinkham, *Group Theory and Quantum Mechanics* (Dover Publications, Mineola, N. Y.) (1964).

[68] S. Choi, V. N. Agafonov, V. A. Davydov, and T. Plakhotnik, *Ultrasensitive All-Optical Thermometry Using Nanodiamonds with a High Concentration of Silicon-Vacancy Centers and Multiparametric Data Analysis*, ACS Photonics **6**, 1387 (2019).

Appendix

A Group Theory and SiV Molecular Basis States

In this section, we will outline how the mathematical discipline of group theory can be used to calculate the basis states of the SiV centre and how the representations of the interaction Hamiltonians in Sect. 1.2.2 are determined. To this end, we follow the description given by Hepp[34] in a cursory manner. The interested reader can find numerous accounts of generalised group theory and its relation to quantum mechanics in the literature.[66,67]

Group theory provides systematic techniques to classify symmetry elements and operations, and its notation includes a compact way of including the symmetry that defines a molecular system by introducing the concepts of point groups, character tables, and representations.[34]

A group is a mathematical object, defined by a set of elements G equipped with a binary operation $\mathrm{G} \times \mathrm{G} \to \mathrm{G}$ such that the following group axioms are fulfilled[66]:

1. $(ab)c = a(bc) \quad \forall a, b, c \in \mathrm{G}$ (Associativity)
2. $\exists e \in \mathrm{G}$ such that $ea = ae = a \quad \forall a \in \mathrm{G}$ (Identity)
3. $\forall a \in \mathrm{G} \quad \exists a^{-1} \in \mathrm{G}$ such that $a^{-1}a = aa^{-1} = e$ (Inverse).

In this treatment, we restrict ourselves to finite groups. If the operation of the group is commutative, that is, $ab = ba \quad \forall a, b \in \mathrm{G}$, then the group is said to be commutative or Abelian.

Symmetry elements and point groups

An example of a group is the special orthogonal group SO(2), also called the rotation group in two dimensions. Its elements are the rotations around a point. We can apply a rotation to an object in space, for example an equilateral triangle. If we apply a rotation of 120° around the midpoint of the triangle, the resulting triangle is indistinguishable from the original triangle (except when we label its corners). We call such an operation a *symmetry operation*, performed with respect to a certain *symmetry element*. In our example, the symmetry element is the midpoint of the triangle, about which the rotation is applied. The symmetry elements of an object constitute a group.

For the SiV defect centre, we have four classes of symmetry elements in addition to the trivial symmetry element, the identity (which leaves the object unchanged)[34]

1. **Rotation axes** - The SiV centre has a three-fold rotation axis denoted C_3 and three two-fold rotations axes denoted C_2, C_2', and C_2''. Generally, a C_n rotation axis generates the symmetry operations of n rotations by multiples of $(360/n)°$. The rotation axis of the highest order n is the main axis of the defect, which is why the SiV centre is also referd to as a trigonal ($n = 3$) defect.

2. **Mirror planes** - There are three mirror planes for the SiV centre, each generating a reflection symmetry operation, denoted with σ. A vertical mirror plane that bisects two C_2 axes is called a dihedral plane. The three planes of the SiV are of this nature and are called σ_d, σ_d', and σ_d''.

3. **Centre of inversion** - The centre of inversion generates the inversion operation denoted with i, which negates every point of the defect $(x, y, z) \rightarrow (-x, -y, -z)$. Although inversion is not a fundamental symmetry operation (that is, it can be constructed from other symmetry operations), it is often listed as one due to its importance. The wave functions of a defect that shows inversion symmetry like the SiV are labelled with the parity labels even (g) and odd (u). The labels 'g' and 'u' originate from the German translations of the parity labels ('gerade' and 'ungerade').

4. **Improper rotation axes** - The SiV exhibits one S_6 improper rotation axis, coinciding with the C_3 rotation axis. The corresponding symmetry operation is a combination of a rotation about a C_n rotation axis and a reflection at a mirror plane σ perpendicular to this axis (and although it consists of a combination, it is considered a unique operation). In general, an improper rotation axis is denoted S_n, where n corresponds to a $(360/n)°$ rotation axis. In the case of the SiV, the S_6 symmetry axis only generates two new symmetry operations, since some of its inherent symmetry operations are already found in previous operations. For example, $S_6^2 = C_3^1$ (superscripts denote the multiples of $(360/n)°$).

The symmetry of a defect can be classified by listing all of its symmetry elements, but this is in general impractical, especially if the defect under investigation is highly symmetric. Hence we can define collections of symmetry elements and corresponding operations that classify a defect unambiguously. Such a collection is called a *point group* (from the fact that all symmetry elements of a defect pass through at least one point that is unchanged when operations are applied to the defect). The SiV is accordingly assigned to the D_{3d} point group, with one C_3 axis, three C_2 axes and three σ_d mirror planes (cf. Hepp, p. 29 for a flow-chart to justify this assignment[34]). This point group contains 12 symmetry operations that fulfil the group axioms from above.

Representations and Characters

We are now ready to step from the realm of illustrative geometrical interpretations of the symmetry operations to a more abstract, mathematical treatment. The symmetry operations can be described by numerical operators, which again form a group. This group, which we denote with Γ, is called a *representation* of the original group of symmetry operations G, and here, we associate to each member $A \in \mathrm{G}$ a square matrix $\Gamma(A)$, thereby defining the group homomorphism mapping the group of symmetry operations to the group of its representations. For the representation it holds that $\Gamma(A)\Gamma(B) = \Gamma(AB) \quad \forall A, B \in \mathrm{G}$.

To generate a representation of a point group we can investigate the effect that symmetry operations have on a set of basis vectors $\{\hat{x}, \hat{y}, \hat{z}\}$ of three dimensional space. For example, the C_3^1 operation, corresponding to a 120° rotation about the high symmetry axis, defines in this basis the matrix:

$$\Gamma(C_3^1) = \begin{pmatrix} -\frac{1}{2} & -\frac{1}{2}\sqrt{3} & 0 \\ \frac{1}{2}\sqrt{3} & -\frac{1}{2} & 0 \\ 0 & 0 & 1 \end{pmatrix}.$$

The matrices constructed in this way act as follows: Let us say that one of the next-neighbour carbon atoms constituting the SiV as coordinates $\vec{r} = (x, y, z)$. Applying a symmetry operation $A \in G$ (for example, C_3^1), will change the coordinates of this atom according to $\Gamma(A)\vec{r} = \vec{r}'$.

However, we note that representations of a group are not unique; we could have chosen a different basis to construct our matrix from above, and we can transform it to different bases using any unitary operation. Both of these ways to obtain a different representation results in an equally valid representation of the point group D_{3d}.[66] To unambiguously characterise the representations corresponding to a symmetry operation, we need a feature that does not depend on which which representation we choose. We therefore define the *character* $\chi^{(j)}(A)$ of a representation j under the symmetry operation A as the trace of the square matrix $\Gamma^{(j)}(A)$ of this representation. The trace of a matrix is invariant under unitary transformations, and thus the ambiguity is eliminated.

Another important concept regarding representations is *reducibility*. A representation can sometimes be decomposed into different, but equally valid, representations of smaller dimension. It turns out that all symmetry operations A of the D_{3d} point group have block diagonal form in the basis we have chosen:

$$\Gamma(A) = \left(\begin{array}{cc|c} \multicolumn{2}{c|}{\multirow{2}{*}{$\Gamma^{(1)}(A)$}} & 0 \\ & & 0 \\ \hline 0 & 0 & \Gamma^{(2)}(A) \end{array}\right),$$

meaning, it contains two representations $\Gamma^{(1)}(A)$ and $\Gamma^{(2)}(A)$ of dimension 2 and 1. Therefore, $\Gamma(A)$ is reducible. $\Gamma^{(2)}(A)$ is irreducible since 1 is the lowest dimension. To check whether a representation is reducible, we can try to find a transformation that converts all of the matrices of one representation into block diagonal form. If such a transformation exists, the representation is reducible, and irreducible if no such transformation exists. A reducible representation Γ can then be written as a linear combination of irreducible representations Γ_{IR}:

$$\Gamma = \sum_j a_j \Gamma_{\mathrm{IR}}^{(j)},$$

where a_j determine how often the irreducible representation $\Gamma_{\mathrm{IR}}^{(j)}$ appears in Γ. Hence, for our example, we have $\Gamma = 1 \cdot \Gamma^{(1)} + 1 \cdot \Gamma^{(2)}$.

Character tables

The characters χ of the different representations of a point group are summarised in *character tables*, and can be found in the literature (cf. Tab. 2 for the D_{3d} table).[67] In these tables, we can find the characters that we calculate for different symmetry classes (top row of Tab. 2), i.e. the traces of the matrices of these symmetry classes, which assigns irreducible representations to the case under investigation (left most column of Tab. 2). Mulliken symbols are used to describe the representations. The letters A, B, E, T refer to the dimensionality of an irreducible representation. A, B refer to one-dimensional symmetric and anti-symmetric (with respect to the main C_n operations) representations, E refers to two-dimensional representation (we can see that $\Gamma^{(1)} = E_u$ from above), and T are three-dimensional. The subscript g and u refer again to even and odd parity, denoting the sign of the character of the inversion operation. Finally, the subscript 1 and 2 refer to the sign of the character under C_2 rotations. $\Gamma^{(2)}$ in our example from before can be attributed to A_{2u}. There are also generating functions for representations, for example, A_{2u} is generated by z and E_u by the pair (x,y). Additionally, there are also representations generated by quadratic functions, such as $x^2 + y^2$ for A_{1g}. These generating functions (listed in the two right most columns of Tab. 2) are called basis functions and play an important role in group theory in a quantum mechanical context.

D_{3d}	E	$2C_3$	$3C_2$	i	$2S_6$	2σ	linear, rotations	quadratic
A_{1g}	1	1	1	1	1	1		$x^2 + y^2, z^2$
A_{2g}	1	1	-1	1	1	-1	R_z	
E_g	2	-1	0	2	-1	0	(R_x, R_y)	$(x^2 - y^2, xy), (xz, yz)$
A_{1u}	1	1	1	-1	-1	-1		
A_{2u}	1	1	-1	-1	-1	1	z	
E_u	2	-1	-2	-2	1	0	(x, y)	

Tab. 2: Character table of the D_{3d} point group.

Quantum Mechanics and Group Theory

Let us now consider a physical system S that is left invariant by the operations of a group G. This means, G is the symmetry group of the system S. S is described by Schrödinger's equation $\hat{H}\psi^{(n)} = E_n\psi^{(n)}$, with the Hamiltonian $\hat{H}$, an arbitrary wave function $\psi^{(n)}$ and its corresponding energy E_n. We now define operators generated by elements of the symmetry group $A \in G$ of S, which we call P_A, such that:

$$P_A f(\vec{r}) = f(A^- 1\vec{r}).$$

$\vec{r}$ marks the position of a point P of the system, and $f(\vec{r})$ is an arbitrary function of $\vec{r}$. With this definition, one can prove that the group of P_A is isomorphic to the symmetry group G, and that the operators P_A commute with the Hamiltonian of the system. This is a generalisation of the idea that the kinetic and potential energies of a defect or molecule that has a symmetry group G are invariant with respect to G.[66] Applying this theorem to Schrödinger's equation it is easy to see that if $\psi^{(n)}$ is an eigenfunction of $\hat{H}$ to the eigenvalue E_n, so is $P_A\psi^{(n)} = \phi^{(n)}$:

$$P_A\hat{H}\psi^{(n)} = P_A E_n\psi^{(n)} \Leftrightarrow \hat{H}P_A\psi^{(n)} = E_n P_A\psi^{(n)}.$$

We call the group of the operators P_A *the group of Schrödinger's equation*.

We have seen that the matrices $\Gamma(A)$ of the symmetry operations A are considered representations of the symmetry group of a defect. We can now combine the concepts of irreducible representations and the group of Schrödinger's equation.[34] Let E_n be a l_n-fold degenerate eigenvalue of $\hat{\mathrm{H}}$, with a set of l_n mutually orthogonal eigenfunctions $\psi_\kappa^{(n)}$, $\kappa = 1, ..., l_n$. Applying an operator P_A out of the group of Schrödinger's equation to a particular eigenfunction $\psi_\nu^{(n)}$, we obtain a new function that has the same energy. This new function can be expressed as a linear combination of the eigenfunctions $\psi_\kappa^{(n)}$. We can therefore write this new function in terms of a multiplication with a matrix $\Gamma^{(n)}(A)$[34]:

$$P_A \psi_\nu^{(n)} = \sum_{\kappa=1}^{l_n} \psi_\kappa^{(n)} \left[\Gamma^{(n)}(A)\right]_{\kappa\nu} .$$

In this manner, we have constructed a representation $\Gamma^{(n)}(A)$ for the group of Schrödinger's equation using the eigenfunctions as generating functions, much like we have seen that z generates A_{2u} and (x, y) generate E_u. The set of l_n degenerate eigenfunctions $\psi_\kappa^{(n)}$ form a basis for the l_n-dimensional irreducible representation $\Gamma^{(n)}$.

This is the reason why quantum mechanical levels are labelled according to their symmetry: The irreducible representations of the group of Schrödinger's equation correspond to the eigenfunctions of the physical system S, and thus label the corresponding states as well as specifying their degeneracy.

However, often the eigenfunctions of a physical system are not known explicitly. But since there is a correspondence between the eigenstates and the irreducible representations of a system, which can be constructed from symmetry arguments, we can obtain the eigenfunctions of the SiV centre with group theory.

SiV Basis States

As outlined in Sect. 1.2.1, the molecular structure of the SiV centre is such that it has six next-neighbouring carbon atoms next to the bond-central silicon atom, and we consider the SiV as an individual molecule. These carbon atoms thus have dangling, unsaturated bonds. Based on this, we can derive a reducible representation according to this structure and the dangling-bond orbitals. Then, we can decompose this representation into a irreducible representation and use the character table of the $D_{3\mathrm{d}}$ point group to derive the *symmetry adapted linear combinations* (SALC) of the dangling bond orbitals. SALCs are effective orbitals that are formed by a superposition of the dangling bond orbitals. The SALCs of the SiV, then, correspond to the basis states that we use for the perturbation calculations in Sect. 1.2.2.[34]

The effective decomposition of the representation of the dangling bond orbitals yields the result

$$\Gamma^{(\sigma)} = A_{1\mathrm{g}} + E_{\mathrm{g}} + A_{2\mathrm{u}} + E_{\mathrm{u}},$$

where the superscript σ refers to the fact that the nature of the bonds are σ-type (the strongest covalent bonds), as the carbon atoms are sp^3-hybridized.[34] Thus, we denote the dangling bond orbitals of six nearest-neighbour carbon atoms as σ_k and σ_k', $k \in \{1, 2, 3\}$. This decomposition shows that there will be four electronic states for

the SiV centre. The A-type representations are, as mentioned before, one-dimensional, and thus correspond to non-degenerate electronic states. The E-type representations signify two-fold degenerate states.

In the next step, we need to project out the basis functions from the dangling bond orbitals σ_k and σ'_k by applying the projection operator $\mathcal{R}^j$ to them. This operator is defined with the characters $\chi^{(j)}_{\mathrm{IR}}(A)$ of the irreducible representations $\Gamma(A)$ that we found in the decomposition from before:

$$\mathcal{R}^j = \frac{1}{N}\sum_A \left[\chi^{(j)}_{\mathrm{IR}}(A)\right]^* P_A,$$

where N is a normalisation factor and P_A is the operator of the group of Schrödinger's equation corresponding to the symmetry operation A. This brings us to the dangling bond SALCs of the SiV, which are denoted according to their corresponding irreducible representation, but with lower-case letters to distinguish them from the irreducible representations. As we mentioned before, the E-type representations are two-dimensional and thus require two SALCs each, which we write $e_{\mathrm{u}x}$ and $e_{\mathrm{u}y}$ for E_{u} and analogously for E_{g}. Thus we have the six dangling bond SALCs of the carbon atoms of the SiV defect[34]:

$$\begin{aligned}
a_{1\mathrm{g}} &= \frac{1}{\sqrt{6}}(\sigma_1+\sigma_2+\sigma_3+\sigma'_1+\sigma'_2+\sigma'_3)\\
a_{2\mathrm{u}} &= \frac{1}{\sqrt{6}}(\sigma_1+\sigma_2+\sigma_3-\sigma'_1-\sigma'_2-\sigma'_3)\\
e_{\mathrm{g}x} &= \frac{1}{\sqrt{12}}(2\sigma_1-\sigma_2-\sigma_3+2\sigma'_1-\sigma'_2-\sigma'_3)\\
e_{\mathrm{g}y} &= \frac{1}{2}(\sigma_2-\sigma_3+\sigma'_2-\sigma'_3)\\
e_{\mathrm{u}x} &= \frac{1}{\sqrt{12}}(2\sigma_1-\sigma_2-\sigma_3-2\sigma'_1+\sigma'_2+\sigma'_3)\\
e_{\mathrm{u}y} &= \frac{1}{2}(\sigma_2-\sigma_3-\sigma'_2+\sigma'_3).
\end{aligned}$$

In principle, we must also consider the atomic orbitals of the silicon atom. These mix with the SALCs via the Coulomb interaction. It can be shown that this mixing is only present if the silicon orbital belongs to the same irreducible representation of as the dangling bond SALC of the corresponding carbon atom. That is, the mixture of the silicon orbitals and the carbon SALCs have the form:

$$\alpha a_{1\mathrm{g}} + \beta a^{\mathrm{Si}}_{1\mathrm{g}},$$

where α, β quantitatively describe the mixture. *Ab initio* calculations show that the mixing of the silicon orbitals with the dangling bond SALCs is small, $\beta \ll 1$,[33] and we therefore decide to neglect it. Thus, as an approximation, we describe the SiV states as only the SALCs of the dangling carbon bonds.

Further, Gali and Maze[33] show that the ordering of the orbitals is, from lowest to highest energy, $a_{1\mathrm{g}}\ a_{2\mathrm{u}}\ e_{\mathrm{u}}\ e_{\mathrm{g}}$. Filling these orbitals with the eleven electrons of the SiV, also taking spin degeneracy into account, we get the configuration $a^2_{1\mathrm{g}}a^2_{2\mathrm{u}}e^4_{\mathrm{u}}e^3_{\mathrm{g}}$ for the ground state. Thus, there is an electron hole in the $e_{\mathrm{g}x}$ or $e_{\mathrm{g}y}$ orbitals[34] and we denote the ground state $^2\mathrm{E}_{\mathrm{g}}$. By assuming that the zero-phonon line (ZPL) transition of the defect at 737 nm occurs when an electron is excited to the $e_{\mathrm{g}x}$ or $e_{\mathrm{g}y}$ orbital, the excited state is called $^2\mathrm{E}_{\mathrm{u}}$ and its configuration

is $a_{1g}^2 a_{2u}^2 e_u^3 e_g^4$.
The electron hole can take any of the four positions of e_g or e_u in both the ground and the excited state, expressing the four-fold degeneracy of the SiV (cf. Fig. 13). These four positions correspond to basis vectors, and thus we obtain the bases for ^2E_g and ^2E_u in Dirac notation[34]:

$$^2E_g \rightarrow \{|e_{gx}\uparrow\rangle, |e_{gx}\downarrow\rangle, |e_{gy}\uparrow\rangle, |e_{gy}\downarrow\rangle\}$$
$$^2E_u \rightarrow \{|e_{ux}\uparrow\rangle, |e_{ux}\downarrow\rangle, |e_{uy}\uparrow\rangle, |e_{uy}\downarrow\rangle\}.$$

These are the basis states that we use for the perturbation calculations in Sect. 1.2.2.

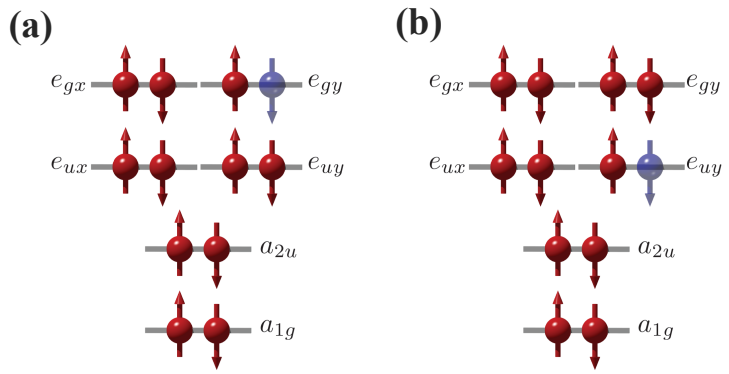

Fig. 13: Ground **(a)** and excited **(b)** state configurations of the SiV centre. Red arrows label electrons, blue arrows electron holes. Adapted from Hepp.[34]

It remains to be seen what the matrix elements of our interaction Hamiltonians look like in these bases.

Interaction Matrix Elements

Group theory can also be used to deduce whether a matrix element, for example of the form $\langle\psi_i|\hat{H}|\psi_j\rangle$, must vanish for symmetry reasons. That is, if the matrix element is not invariant under operations of the group of Schrödinger's equation, it is zero. Further, the matrix element calculation of $\langle\psi_i|\hat{H}|\psi_j\rangle$ can be replaced by the direct product of the representations of ψ_i, ψ_j, and $\hat{H}$ (which we call $\Gamma^{(i)}, \Gamma^{(j)}$ and $\Gamma^{(k)}$) such that[34]

$$\langle\psi_i|\hat{H}|\psi_j\rangle = \Gamma^{(i)} \otimes \Gamma^{(k)} \otimes \Gamma^{(j)}.$$

To compute the direct product of two matrices (that is, in our case, our representations), we multiply each element of $\Gamma^{(k)}$ with each element $\Gamma^{(j)}$. We encountered such a product when we extended the Jahn-Teller Hamiltonian, a purely orbital interaction, to spin space in Eq. (1.2). A direct product of representations is again a representation. Further, we can also define a direct product of the characters χ of irreducible representations, which is just the usual multiplication of the characters. That is, the character of a irreducible representation obtained by a direct product is the product of the characters of the individual irreducible representations. In equations, if we have irreducible representations $\Gamma^{(A)}, \Gamma^{(B)}$, and $\Gamma^{(C)} = \Gamma^{(A)} \otimes \Gamma^{(B)}$, then:

$$\Gamma^{(A)} \otimes \Gamma^{(B)} = \Gamma^{(C)} \Rightarrow \chi^{(C)} = \chi^{(A)}\chi^{(B)}.$$

If a direct product of irreducible representations results in a reducible representation, we can decompose it into a

sum of irreducible representations. This gives us computational rules for which representation will result from a direct product of representations. For example, the direct product $\mathrm{E_g} \otimes E\mathrm{u} = A_{1\mathrm{u}} + A_{2\mathrm{u}} + \mathrm{E_u}$, or $A_{1\mathrm{u}} \otimes \mathrm{E_g} = \mathrm{E_u}$.[34] A matrix element will vanish for symmetry reasons if it does not contain the totally symmetric representation A_1. Thus we can deduce which matrix elements must be zero due to symmetry, however, group theory fails to provide the value of the matrix elements that do not vanish.

As an example, let us consider the orbital angular momentum operator $\hat{\vec{\mathrm{L}}} = (\hat{\mathrm{L}}_x, \hat{\mathrm{L}}_y, \hat{\mathrm{L}}_z)$, whose matrix form we need to construct the spin-orbit interaction Hamiltonian $\hat{\mathrm{H}}^{\mathrm{SO}}$ in Eq. (1.1). Its matrix elements are of the form $\langle e_\mathrm{g}| \hat{\vec{\mathrm{L}}} |e_\mathrm{g}\rangle$ or $\langle e_\mathrm{u}| \hat{\vec{\mathrm{L}}} |e_\mathrm{u}\rangle$. The matrix elements of the components of $\hat{\vec{\mathrm{L}}}$ do not vanish for symmetry reasons, and thus, we need to employ a different strategy to compute them. The states e_x and e_y for both the excited and ground state have similarities to the p_x and p_y orbitals of an atom (and p_z is similar to $a_{2\mathrm{u}}$).[34] These p-orbitals form together the spherical harmonics $Y_l^{m_l}$ with $l = 1$ and $m_l \in \{-1, 0, 1\}$, which are eigenstates of the $\hat{\mathrm{L}}_z$ operator. In analogy to $Y_l^{m_l}$, we introduce the states $e_+ = -\frac{1}{\sqrt{2}}(e_x + \mathrm{i}e_y)$ and $e_- = \frac{1}{\sqrt{2}}(e_x - \mathrm{i}e_y)$. These states are eigenstates of $\hat{\mathrm{L}}_z$ as well, with $\hat{\mathrm{L}}_z e_\pm = \pm\hbar e_\pm$, and thus we can write the matrix elements of $\hat{\mathrm{L}}_z$ in the $e_\pm$ basis (in units of $\hbar$):

$$\hat{\mathrm{L}}_z \doteq \begin{pmatrix} 1 & 0 \\ 0 & -1 \end{pmatrix}.$$

The off-diagonal terms are zero as e_+ and e_- are orthogonal. We can additionally define the operators $\hat{\mathrm{L}}_\pm = \hat{\mathrm{L}}_x \pm \hat{\mathrm{L}}_y$, with

$$\begin{aligned} \mathrm{L}_+ Y_l^{m_l} &= \hbar\sqrt{(l - m_l)(l + m_l + 1)}\, Y_l^{m_l+1} \\ \mathrm{L}_+ Y_l^{m_l} &= \hbar\sqrt{(l + m_l)(l - m_l + 1)}\, Y_l^{m_l-1}. \end{aligned}$$

These operators couple the $e_\pm$ states to the $a_{2\mathrm{u}}$ state, but they introduce no coupling between the $e_\pm$ states themselves. Hence, the matrix representation of $\hat{\mathrm{L}}_\pm$ in the $e_\pm$ basis is identical to the zero matrix in two dimensions. It is easy to see that there exists a simple linear transformation between the $e_\pm$ basis and the $e_{x,y}$ basis, given by

$$\hat{T} = \begin{pmatrix} -1 & -\mathrm{i} \\ 1 & -\mathrm{i} \end{pmatrix}.$$

The components of $\hat{\vec{\mathrm{L}}}$ can then be transformed from the $e_\pm$ basis to the $e_{x,y}$ basis of the dangling bond SALCs according to

$$\hat{\mathrm{L}}_{x,y,z}^{(e_{x,y})} = \hat{T}^{-1} \hat{\mathrm{L}}_{x,y,z}^{(e_\pm)} \hat{T}. \tag{1}$$

Since $\hat{\mathrm{L}}_\pm^{(e_\pm)}$ are identical to zero, so are $\hat{\mathrm{L}}_{x,y}$ in both bases. Hence we arrive at the representations of the orbital angular momentum operators in the basis of the dangling bond SALCs of the SiV centre

$$\hat{\mathrm{L}}_x \doteq \begin{pmatrix} 0 & 0 \\ 0 & 0 \end{pmatrix} \qquad \hat{\mathrm{L}}_y \doteq \begin{pmatrix} 0 & 0 \\ 0 & 0 \end{pmatrix} \qquad \hat{\mathrm{L}}_z \doteq \begin{pmatrix} 0 & \mathrm{i} \\ -\mathrm{i} & 0 \end{pmatrix}.$$

With the components of $\hat{\vec{\mathrm{L}}}$ at hand, we can write the Spin-orbit Hamiltonian

$$\hat{\mathrm{H}}^{\mathrm{SO}}_{\mathrm{g,e}} = \lambda_{\mathrm{g,e}} \hat{\vec{\mathrm{L}}} \cdot \hat{\vec{\mathrm{S}}} = \lambda_{\mathrm{g,e}} \hat{\mathrm{L}}_z \cdot \hat{\mathrm{S}}_z \doteq \frac{\mathrm{i}\lambda_{\mathrm{g,e}}}{2} \begin{pmatrix} 0 & 0 & 1 & 0 \\ 0 & 0 & 0 & -1 \\ -1 & 0 & 0 & 0 \\ 0 & 1 & 0 & 0 \end{pmatrix},$$

as presented in Eq. (1.1) in Sect. 1.2.2 (where we have used the fact that $\hat{\mathrm{S}}_z$ is diagonal in this basis).

Other interaction terms (such as the dipole operators in Eq. (1.6)) can be derived in a similar manner, and we refer to the descriptions given by Hepp[34] and Becker[35] for further details.

B φ-Dependence of the Numerical Model

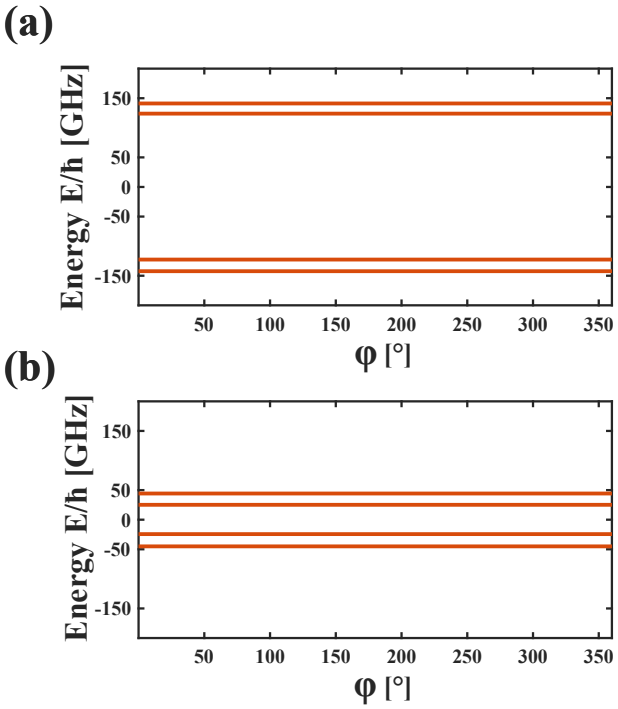

Fig. 14: **(a)** and **(b)** Exemplary calculation of the excited (a) and ground (b) state electronic level structure of the SiV centre in dependence of the azimuthal angle φ in spherical coordinates. The other coordinates in this case are $\|B\| = 1.5\,\mathrm{T}$, $\theta = 109.7°$. The slope of the lines does however not depend on the other coordinates, it is always zero.

Fig. 14 shows an exemplary calculation of the excited (a) and ground (b) state electronic level structure of the SiV centre in dependence of the azimuthal angle φ of the magnetic field to the high-symmetry axis of the SiV coordinates. Varying this angle does not produce an effect on the level structure, which is why we set it to arbitrary values. This effect persists also for different values of the other two coordinates ($\|B\|$, θ).

C Temperature Sensing with the SiV Centre

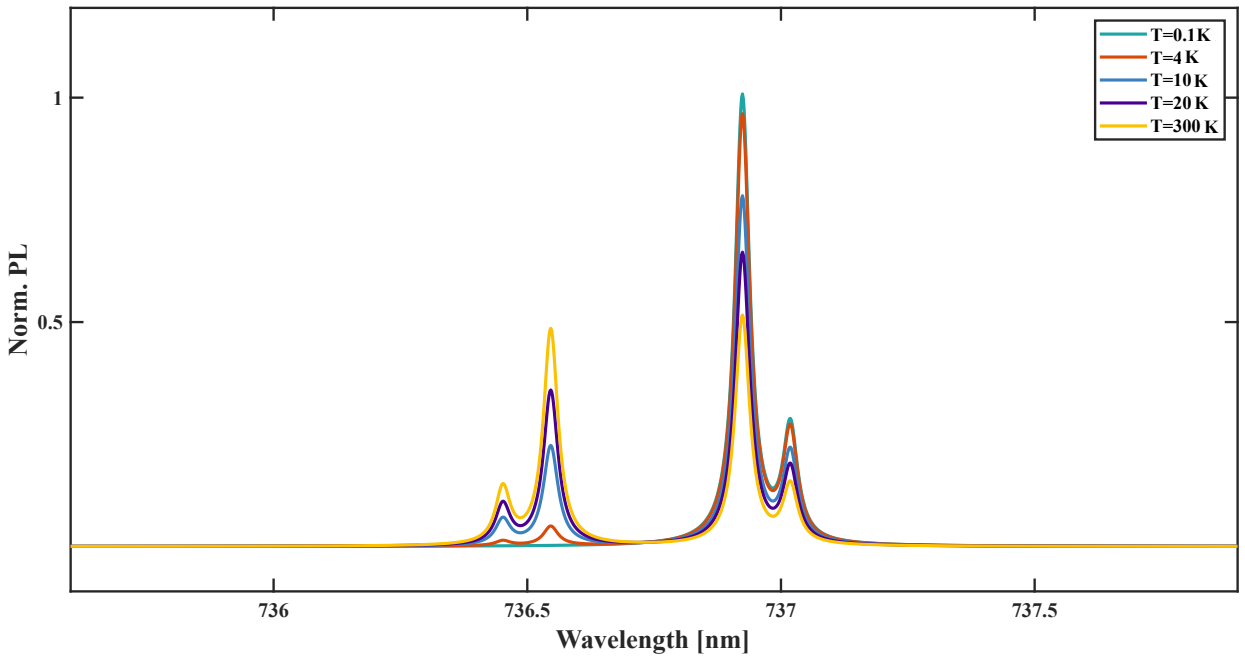

Fig. 15: Calculated optical spectra for different temperatures of the diamond lattice according to the model presented in Sect. 1.2.2. The fact that the intensity distribution of the four fine-structure peaks in the optical spectrum depends on the temperature can be used for temperature sensing. We note that the model presented here does not take thermal broadening of the lines into account.

In Fig. 15, temperature dependent optical spectra calculated from the model presented in Sect. 1.2.2 are depicted. This behaviour enables gauging the temperature of the diamond lattice under investigation, presenting a useful tool to easily estimate the quality of the thermalisation with the cryostat. All-optical thermometry has been demonstrated for the SiV centre at room temperature.[68] The thermalisation effect discussed in the main text can be used to employ the SiV in low-temperature thermometry by monitoring the relative intensity between the transitions from the lower excited state and the upper excited state. Since the splitting between the two excited states is of the order of $\Delta E_e \sim$250 GHz, we expect that the SiV is an effective thermometer up to temperatures of $\hbar/k_B \cdot \Delta E_e \sim 12$ K. In Fig. 15, however, the difference between a temperature of 10 K and 20 K can still easily be distinguished. This can be attributed to the fact that the model is relatively simple, and further studies are required to quantitatively investigate this phenomenon. Yet this effect and the calculations presented in this thesis can already serve as qualitative estimates of the temperature of the diamond lattice. We also note that other thermal effects, such as for example thermal broadening, have been neglected in the model.

D Saturation Curve

To characterise the optical properties of the SiV centres in our nano-pillars, saturation curves were recorded, an example of which is depicted in figure 16.

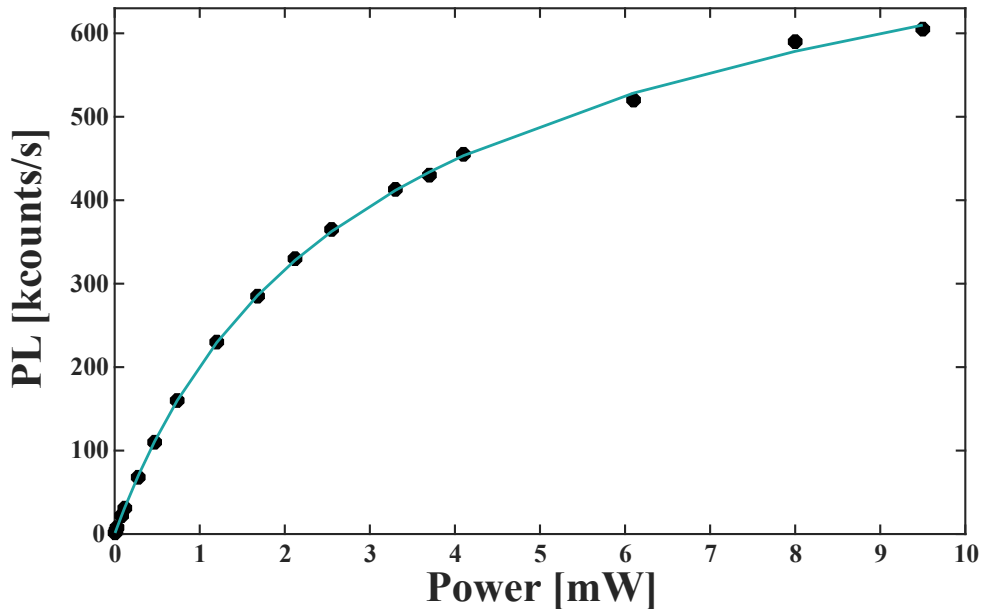

Fig. 16: Exemplary saturation curve of an SiV Centre, with data in black dots and the fit given by Eq. (2) in mint. This particular example was recorded before the second anneal. The fit determines the saturation power P_{Sat} to be 2.5 mW, the saturation counts I_{Sat} to be 360 kcounts/s, and the background-counts B to be 7.4 kcounts/(mW s).

The fluorescence rate I of an emitter driven with laser power P is

$$I = I_\infty \frac{P}{P + P_{Sat}} + B \cdot P, \tag{2}$$

with I_∞ the maximum fluorescence rate, P_{Sat} the saturation power and B background-counts.[57] Additionally, we can extract the background-correction factor for the $g^{(2)}(t)$ analysis by defining the correction factor ρ

$$\rho = \frac{I_{Sat}}{I_{Sat} + B \cdot P_{Sat}}, \tag{3}$$

and thus obtain the background corrected $g^{(2)}(t)$

$$g^{(2)}(t)_{corr} = \frac{g^{(2)}(t) - (1 - \rho^2)}{\rho^2}.\,^{56} \tag{4}$$

E Matlab Code

```
%% SiV Physics Simulation

%This code can be used to simulate basic SiV physics. Implemented are
%routines for the Hamiltonians, the transition frequencies and
%zero-field spectra including intensities.

% angle between high symmetry axis of SiV and magnetic field (in degree)
theta = 54.7;

%temperature in of the diamond lattice (in Kelvin)
Temp = 8.5;

%Generate Eigenvectors
[Hg,He] = Hamiltonian('SOZeeman',0.1,theta,0);
[Vg,DHg] = eig(Hg);
[Ve,DHe] = eig(He);

%Dipole operators
    pxtemp = [1 0 ; 0 -1];
    pytemp = [0 -1; -1 0];
    pztemp = [2 0; 0 2];
%Extend to spin-space
    P(:,:,1) = kron(pxtemp,eye(2)); %px
    P(:,:,2) = kron(pytemp,eye(2)); %py
    P(:,:,3) = kron(pztemp,eye(2)); %pz

%Transitions:
% The vector f contains the transitions. 1,3 means we look at the
% transition of eigenvector 1 of the groundstate manifold to eigenvector 3
% of the excited state manifold. They are ordered A,B,C,D.
f = [2,4; 3,3; 1,2; 4,1];
g = [1,4; 3,4; 1,1; 4,2];
b = [2,3; 4,3; 2,1; 3,1];
r = [1,3; 4,4; 2,2; 3,2];

%Vectors g,b,r contain basically the same information, but for all possible
%transitions, since we don't know which of the states is spin up or down.
%If we knew, we could just select the transitions that are spin-allowed. We
%do this and sum up all the contributions.

%Prepare structure for all polarisations. Rows are the transition, columns
```

```
%are px, py, pz.
Inten = zeros(4,3);

%Calculate transition matrix elements <Vg|P|Ve> and their respective
%intensities
for k = 1:4
    for i=1:3
        trans1 = Vg(:,f(k,1))'*P(:,:,i)*Ve(:,f(k,2));
        trans2 = Vg(:,g(k,1))'*P(:,:,i)*Ve(:,g(k,2));
        trans3 = Vg(:,b(k,1))'*P(:,:,i)*Ve(:,b(k,2));
        trans4 = Vg(:,r(k,1))'*P(:,:,i)*Ve(:,r(k,2));
        Inten(k,i) = abs(trans1 + trans2 + trans3 + trans4)^2; %Sum up all intensities
            for the spectrum
    end
end

%Simulate the spectrum:
%Calculate the intensities of the peaks

Inten2 = zeros(1,4);
eta = [1 1 1]; %collection efficiencies in x,y,z direction
for k=1:4
   for i=1:3
    Inten2(k) = Inten2(k)+eta(i)*Inten(k,i);
   end
end

[n1,n2] = TempDep(Temp);
Inten2 = Inten2./max(Inten2);
Inten2(1) = n2*Inten2(1);
Inten2(2) = n2*Inten2(2);
Inten2(3) = n1*Inten2(3);
Inten2(4) = n1*Inten2(4);

%Calculate the position of the peaks
dataEg = diag(DHg);
dataEe = diag(DHe);

l = ['A','B','C','D'];
pos = zeros(1,4);
for i=1:4
    M = getTransitionFreqData(l(i),dataEg',dataEe');
```

```
    pos(i) = 3*10^8/(M(1,1)+4.07202*10^(14))*10^9;%Extract the position of the peak in
        nm. The 10^14 corresponds to 740nm
end

% Plotting routines are omitted for clarity.

%--------------------Zeeman Spectra---------------------- %


%Calculate the eigenvalues and the eigenvectors for each value of the
%magnetic field.
%It's kind of problematic that we don't know which eigenvectors correspond
%to which eigenvalue. We use eigs for this reason, which sorts the
%eigenvalues

tempvec = zeros(4,4);
for i=1:length(Bvalues)
    [Hg,He] = Hamiltonian('All',0.1,theta,45,Bvalues(i));
    [VeBtemp,DHeB] = eigs(He,4,'largestabs'); %eigs, as opposed to eig, sorts the
       eigenvalues from highest magnitude to lowest (unless otherwise specified) and
       the eigenvectors in the same fashion.
    [VgBtemp,DHgB] = eigs(Hg,4,'largestabs');
    dataEeBfield(i,:) = diag(DHeB); %write eigenvalues to matrices
    dataEgBfield(i,:) = diag(DHgB);
    %Reorder eigenvectors (from the dataEeBfield etc we can see, that columns 2 and 4
       need to be switched. same applies to the vectors, hopefully):

    tempvec(:,1) = VeBtemp(:,2);
    tempvec(:,2) = VeBtemp(:,4);
    tempvec(:,3) = VgBtemp(:,2);
    tempvec(:,4) = VgBtemp(:,4);

    VeBtemp(:,2) = tempvec(:,2);
    VeBtemp(:,4) = tempvec(:,1);
    VeBtemp(:,2) = tempvec(:,4);
    VeBtemp(:,4) = tempvec(:,3);

    VeB(:,:,i) = VeBtemp; %write eigenvectormatrices into the array
    VgB(:,:,i) = VgBtemp;
end

temp = zeros(length(Bvalues),4);
```

```
temp(:,1) = dataEeBfield(:,2);
temp(:,2) = dataEeBfield(:,4);
temp(:,3) = dataEgBfield(:,2);
temp(:,4) = dataEgBfield(:,4);

dataEeBfield(:,2) = temp(:,2);
dataEeBfield(:,4) = temp(:,1);
dataEgBfield(:,2) = temp(:,4);
dataEgBfield(:,4) = temp(:,3);

eta = [1 1 1];
%Calculate transition strengths:
Inten = zeros(length(Bvalues),4,4);
for q = 1:length(Bvalues)
    for t=1:4
        for k=1:4
            for i=1:3
                Inten(q,t,k) = Inten(q,t,k) + eta(i)*abs(VgB(:,k,q)'*P(:,:,i)*VeB(:,t,
                    q))^2;
                %Inten(q,t,k) = abs(VgB(:,k,q)'*P(:,:,1)*VeB(:,t,q))^2+abs(VgB(:,k,q)
                    '*P(:,:,2)*VeB(:,t,q))^2+abs(VgB(:,k,q)'*P(:,:,3)*VeB(:,t,q))^2;
            end
            % Account for thermalisation
            [n1,n2] = TempDep(Temp,dataEeBfield(1,1),dataEeBfield(q,t))
            Inten(q,t,k) = Inten(q,t,k).*TempDep(Temp,dataEeBfield(1,1),dataEeBfield(q
                ,t));
        end
    end
end

%A note on the ordering: It should now be the case that the first 4 columns
%of Inten(q,:,:) correspond to transitions A1, A2, A3, A4. Columns 5 - 8
%should be B1, B2, B3, B4 etc.

%Normalise:
Inten = Inten/(max(max(max(Inten))));


%Calculate transition freq:
MtransA = 10^-9*getTransitionFreqData('A',dataEgBfield,dataEeBfield);
MtransB = 10^-9*getTransitionFreqData('B',dataEgBfield,dataEeBfield);
MtransC = 10^-9*getTransitionFreqData('C',dataEgBfield,dataEeBfield);
```

```
MtransD = 10^-9*getTransitionFreqData('D',dataEgBfield,dataEeBfield);

width = 10;
x = linspace(-300,300,5000);
spec = zeros(length(Bvalues),length(x));
for q=1:length(Bvalues)
    vD = [0,Inten(q,1,1),MtransD(q,1),width,Inten(q,1,2),MtransD(q,2),width,Inten(q
        ,1,3),MtransD(q,3),width,Inten(q,1,4),MtransD(q,4),width];
    vC = [Inten(q,2,1),MtransC(q,1),width,Inten(q,2,2),MtransC(q,2),width,Inten(q,2,3)
        ,MtransC(q,3),width,Inten(q,2,4),MtransC(q,4),width];
    vB = [Inten(q,3,1),MtransB(q,1),width,Inten(q,3,2),MtransB(q,2),width,Inten(q,3,3)
        ,MtransB(q,3),width,Inten(q,3,4),MtransB(q,4),width];
    vA = [Inten(q,4,1),MtransA(q,1),width,Inten(q,4,2),MtransA(q,2),width,Inten(q,4,3)
        ,MtransA(q,3),width,Inten(q,4,4),MtransA(q,4),width];
    %Now glue them all together:
    spec(q,:) = LorentzFuncN(16,[vD,vC,vB,vA],x);
end

% Plotting routines are omitted for clarity.

% ----------Functions:---------- %

function [Hg, He] = Hamiltonian(Interaction,q,theta,B)
% This function generates the Hamiltonian for a given B field and angle
% theta. With the first argument, you can decide which interactions to
% account for. The options are: All, SOZeeman,JTZeeman, SOJT. To
% get JT or SO alone, just set B to 0 when calling with SOZeeman or
% JTZeeman.

%Spin matrices:
    sx=0.5*[0 1; 1 0];
    sy=1i*0.5*[0 -1; 1 0];
    sz=0.5*[1 0; 0 -1];

%SO-Splitting in gigahertz:
    lg=47*10^9;
    le=257*10^9;
    %q=0.1;

%JT-effect:
    Gxg=8*10^9;
    Gyg=8*10^9;
```

```
    Gxe=16*10^9;
    Gye=16*10^9;

%Gyromagnetic ratios:
    gL=1.3996245*10^10;
    gS=2.799249*10^10;

%Parts of the Hamiltonians
    H0g=kron(eye(2),eye(2));
    H0e=kron(eye(2),eye(2));
    HSOg=kron(-2*lg*sy,sz);
    HSOe=kron(-2*le*sy,sz);
    HJTg=kron((2*Gxg*sz+2*Gyg*sx),eye(2));
    HJTe=kron((2*Gxe*sz+2*Gye*sx),eye(2));

% ----- Full Hamiltonian -----
if strcmp(Interaction,'All')
    Hg = H0g-HSOg+HJTg+zeeman(q,theta,B);
    He = H0e-HSOe+HJTe+zeeman(q,theta,B);
elseif strcmp(Interaction,'SOZeeman')
    Hg = H0g-HSOg+zeeman(q,theta,B);
    He = H0e-HSOe+zeeman(q,theta,B);
elseif strcmp(Interaction,'JTZeeman')
    Hg = HJTg+zeeman(q,theta,B);
    He = HJTe+zeeman(q,theta,B);
elseif strcmp(Interaction,'SOJT')
    Hg = HSOg+HJTg;
    He = HSOe+HJTe;
else
    warning('Not a valid interaction. Choose from: All, SOZeeman,JTZeeman, SOJT, Bare'
        )
end

%Zeeman-Hamiltonian
    function HZ=zeeman(q,theta,B)
        HZ=q*gL*kron((-2*B*cosd(theta)*sy),eye(2))+gS*0.5*kron(eye(2),(2*B*sz*cosd(
            theta)+2*B*sy*sind(theta)*sin(pi/4)+2*B*sx*sind(theta)*cos(pi/4)));
    end
end

%-------------------------------------------------%
function Mtrans = getTransitionFreqData(type,dataEg,dataEe)
```

```
%getTransitionFreq calculates the transition freq.
%Transition freq. are calculated using the eigenvalues of the
%corresponding Hamiltonian. Type indicates which transition branch should be plotted.
%Valid choices are: All,A,B,C,D.

[n,m]=size(dataEe);
Mtrans=zeros(n,m);

l=0;
if strcmp(type,'All') %Plot all transition frequencies
    for k=1:1:m
        for i=1:1:m
            Mtrans(:,i+l)=dataEe(:,k)-dataEg(:,i);
        end
        l=k*m;
    end

elseif strcmp(type,'A')%Plot only transition frequencies associated with A
        f=[4 1; 4 2; 3 1; 3 2];
        %this gives us the columns in the data that we want to subtract when
        %we calculate the trans freq. first column of this 2X4 matrix is ES, second is
            GS.
        %The data is arranged like this (levelnames): ES A B C D; GS: 1 2 3
        %4. So if you want to calculate the freq of A3 you put in f the
        %row: 1 3. For D1: 4 1. etc.
    for k=1:4
        Mtrans(:,k)=dataEe(:,f(k,1))-dataEg(:,f(k,2));
    end

elseif strcmp(type,'B')%Plot only transition frequencies associated with B
        f=[4 3; 4 4; 3 3; 3 4];
    for k=1:4
        Mtrans(:,k)=dataEe(:,f(k,1))-dataEg(:,f(k,2));
    end

elseif strcmp(type,'C')%Plot only transition frequencies associated with C
    f=[1 1; 1 2; 2 1; 2 2];
    for k=1:4
        Mtrans(:,k)=dataEe(:,f(k,1))-dataEg(:,f(k,2));
    end

elseif strcmp(type,'D')%Plot only transition frequencies associated with D
```

```
    f=[1 3; 1 4; 2 3; 2 4];
    for k=1:4
        Mtrans(:,k)=dataEe(:,f(k,1))-dataEg(:,f(k,2));
    end

else
    error('%s is not an allowed transition. Choose from All, A, B, C or D',type)
end
end

%-------------------------------------------------------%

function [n1,n2] = TempDep(T,E1,E2)
    kb = 1.3806*10^(-23); %in J/K
    hbar = 6.62607*10^(-34); %in J*s
    n2=1/(1+(exp(-((E2-E1)*hbar)/(kb*T))));
    n1 = 1-n2;
end
```

University of Basel

Faculty of Science

Declaration on Scientific Integrity
(including a Declaration on Plagiarism and Fraud)

Title of Thesis *(Please print in capital letters)*:

OPTICAL COHERENCE OF COLOUR-DEFECTS IN DIAMOND

First Name, Surname: JOSH ZUBER
(Please print in capital letters)

Matriculation No.: 14-052-112

With my signature I declare that this submission is my own work and that I have fully acknowledged the assistance received in completing this work and that it contains no material that has not been formally acknowledged.

I have mentioned all source materials used and have cited these in accordance with recognised scientific rules.

In addition to this declaration, I am submitting a separate agreement regarding the publication of or public access to this work.

☐ Yes ■ No

Place, Date: Basel, 31.01.2020

Signature: 

Please enclose a completed and signed copy of this declaration in your Bachelor's or Master's thesis .